L-type Side Impact Intersection Crashes: Investigated Through Field Data and OEM FE Simulations

Neal Morgan, Joon Seok Kong, Seok Ho Hong, Bronislaw Gepner, Jason Kerrigan

Abstract Between 2017 and 2022, L-type side-impact collisions accounted for approximately 7% of all intersection crashes in the United States. This study examined injury risks and occupant kinematics in L-type crashes by integrating field-data analysis, a full-scale vehicle-to-vehicle crash test, and finite element (FE) simulations. Crash Investigation Sampling System (CISS) data were used to identify injury patterns and frequencies in side-struck vehicles. Thoracic and lumbar spine injuries represented prevailing AIS2+ and AIS3+ outcomes, and L-type crashes exhibited the highest AIS3+ injury incidence among intersection-related planar-lateral impacts.

An L-type crash test was conducted between a compact SUV and a mid-sized SUV. The struck vehicle's occupant compartment was modelled in an FE environment with driver and front passenger occupants. Hybrid-III 50th percentile male Anthropomorphic Test Devices (ATDs) and Global Human Body Model Consortium (GHBMC) v6.0 human body models (HBMs) were simulated, using the measured 30 km/h ΔV crash pulse and a scaled 52.5 km/h ΔV pulse, to reproduce test kinematics and evaluate predicted injury.

Both surrogates reproduced principal kinematic features of the crash test. Simulated occupant injury predictions were consistent with field data patterns. These findings support continued development of assessment protocols for L-type and rotationally influenced lateral impacts.

Keywords **CISS, Injury risk, Intersection, L-type, Side-impact.**

I. INTRODUCTION

Side impact crashes have been studied extensively, particularly T-type collisions, where a vehicle is struck nearly perpendicularly on the doors or B-pillar, [1–4] for which regulations exist from organizations such as USNCAP and EURONCAP. As of 2006, Chipman *et al.* [5] described L-type intersection crash configurations based on vehicle damage location, defined as "damage to the front of one vehicle and to the left or right front fender of the other OR damage to the left or right front fenders of both vehicles", and reported that these configurations occurred with frequency comparable to T-type crashes. Chipman also reported that the proportions of crash events resulting in injury are approximately equal between L- and T-type crashes. More broadly, L-type crash scenarios are distinct from other side-impacts, with near perpendicular contact occurring on the struck vehicle's lateral surface in the forward lateral quadrant between the headlights and the cowl at the base of the windshield. These crashes are characterized by both linear motion, induced by the striking vehicle, and rotational motion, resulting from the lever arm between the principal direction of force (PDOF) at contact and the struck vehicle's centre of gravity (CG). Other oblique or small-overlap crashes may have similar physics if planar rotation about the vehicle's CG is introduced. L-type crash scenarios are not part of current regulatory efforts in the US or the EU.

Several studies have investigated the influence of automated emergency braking (AEB) systems on crash configurations. Analyses of insurance claims (Sweden) and police-reported crash data (U.S.) showed that AEB-equipped vehicles more frequently exhibit reduced lateral overlap and corner-impact damage patterns, associated with L-type collision geometries [6–8]. This trend has been attributed to avoidance strategies in AEB design and disengagement during turning under driver-controlled input. Subsequent work using predictive models of crash avoidance paths found that straight crossing path front-to-side corner impacts accounted for 31% of predicted crash events [9], and extensions of this approach [10,11] generated representative crash pulses for automated-driving scenarios, one quarter of which were L-type intersection configurations. Together, these studies suggest that deployment of AEB systems may alter crash geometries toward reduced-overlap and corner-impact configurations, increasing the relevance of L-type crash conditions for occupant safety evaluation.

With L-type intersection crashes occurring at frequencies comparable to T-type crashes, and potentially

Neal Morgan is a Postdoctoral Research Associate (+1-434-297-8041, neal.morgan@virginia.edu) in the Center for Applied Biomechanics at the University of Virginia in Charlottesville, VA. Joon Seok Kong was a Postdoctoral Research Associate also at the Center for Applied Biomechanics for the duration of this work. Seok Ho Hong is Senior Research Engineer at Hyundai Motor Company R&D Division, Hwaseong-si, Gyeonggi-do, South Korea. Bronislaw Gepner is Associate Professor of Mechanical and Aerospace Engineering. Jason Kerrigan is Commonwealth Professor of Mechanical and Aerospace Engineering, both in the Center for Applied Biomechanics of the Department of Mechanical and Aerospace Engineering at University of Virginia in Charlottesville, VA.

increasing with AEB deployment, recent simulation studies have investigated occupant injury patterns and severity in these events. A different 2021 study by Leledakis *et al.* [11] performed FE simulations of an L-type collision striking a mid-sized SUV at speeds ranging from 52 km/h to 77 km/h. A SAFER v9.0.1 human body model (HBM) for a 50th percentile male was placed in the right front seat of the occupant compartment model. The study obtained an L-type crash pulse through simulation of car-to-car impacts between the struck mid-sized SUV and a mid-sized station wagon. The pulses covered Z rotation of 332 deg/s and 26.8 g of linear acceleration. The study found that torso posture was strongly influential to kinematic response in side impacts and that the centre console interaction was significant for far-side impacts. Mroz *et al.* [12] also performed a simulation study on L-type intersection crashes in 2022. This work applied the generic acceleration pulses generated by Höschele *et al.* [10] to identify severe occupant loading conditions. The crash pulses included an L-type straight crossing path frontal to corner collision with ΔVs of 36.2 and 40.8 km/h. Again, the SAFER HBM v9 was employed as the occupant model positioned on a semi-rigid and backless generic seat with a generic interior and restraint system. They concluded that the L-type crash scenario at 41 km/h ΔV should be among the cases recommended to supplement current regulatory occupant safety assessments.

Beyond changes in crash frequency and geometry, L-type collisions may also challenge assumptions embedded in current side-impact restraint systems, commonly evaluated under regulatory T-type side-impact loading conditions. Aldaghlas *et al.* [13] discussed variability in real-world crashes from PDOF, ΔV, or impact location influence on the airbag control modules that trigger in-seat side-airbags, potentially preventing deployment. The timing of deployment for passive restraint systems, along with the relative position of occupants, may also impact restraint effectiveness in injury prevention [14]. The PDOF of L-type crashes is not aligned with the struck-vehicle centre of gravity and acts into the front side panels of the vehicle, adding rotational components to the crash acceleration. The combined linear and rotational loading changes occupant kinematics and may alter timing of sensor trigger and optimal timing of deployment for in-seat side-airbags, motivating further investigation of restraint performance under these conditions [15].

In this study, a physical L-type crash test was performed to provide loading environment for finite element occupant simulations. The crash event involved a left-side impact between a striking compact SUV and a struck mid-sized SUV, with both vehicles traveling at 40 km/h. An OEM finite element model of the struck mid-sized SUV was obtained and reduced to an occupant compartment suitable for simulating the L-type crash for a driver and passenger in the front row. Both seating positions were populated with a Hybrid-III 50th percentile male anthropomorphic test device (ATD) for comparison against the physical crash test, and with a GHBMC v6.0 50th percentile male HBM to provide more biofidelic assessment of internal loading and injury risk. The simulated vehicle and occupants were subjected to a 160 ms, 30 km/h ΔV acceleration pulse extracted from the real-world test, and to a pulse scaled to 52.5 km/h ΔV, to examine severity-dependent occupant response.

The objective of the study was to compare the injury frequency, severity, and regional injury patterns observed in field-data analyses of L-type collisions with injury predictions from ATD and HBM simulations in a controlled, representative crash configuration. This study differs from previous work by employing loading boundary conditions from a full-scale L-type crash test against an OEM quality FE vehicle model including detailed seats and restraints. Additionally, interpreting field data from real-world L-type crashes, comparison of simulation to physical crash data, and investigating matching injury patterns in ATD and GHBMC models differs from prior work that has focused on kinematic outcomes and the use of a sole SAFER HBM occupant.

II. METHODS

A. Field Data Analysis

1) Field Data Source and Filtering

A frequency ratio analysis of intersection crash field data between 2017 and 2022 was performed on information obtained from the Crash Investigation Sampling System (CISS) database. CISS data was selected due to the wider scope, relative to CDS, and the completeness of information in terms of the crash-related injuries and the characterization and severity of crash. The dataset was restricted to tow-away, in-transport passenger vehicles and front-row occupants. Intersection-related crashes were identified using the standard CISS crash-location variable, and cases were retained only when the subject vehicle was struck on the left or right lateral surface, crash type categories 87 and 89 for straight paths struck on left or right. Lateral impact location was refined using the Collision Deformation Classification (CDC) code, with L-type side PDOF isolated using the CDC "F" lateral damage zone definition, as seen in Fig. 1. All filtering steps followed a reproducible sequence that first excluded non-intersection and non-lateral cases, then applied struck-vehicle identification, and removed cases where the struck-vehicle experienced roll-over. Finally, occupant-level exclusions were applied to remove cases with pregnant occupants, occupants outside the left and right seats in the front two rows, occupants with unknown injuries, and incomplete sampling-weight records. L-type injury patterns were compared to other lateral impact locations, particularly T-type as that crash type is presently regulated and has been more extensively studied.

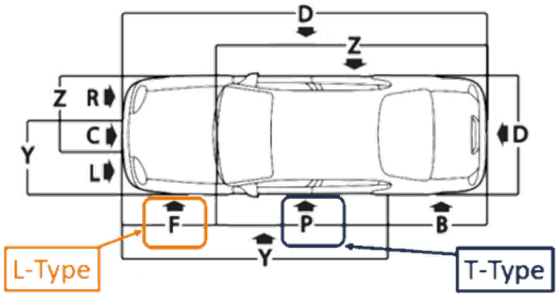

Fig. 1. Collision Deformation Classification (CDC) Diagram

2) Injury Coding and Grouping

Injury severities were based on the Abbreviated Injury Scale (AIS), using the most recent version associated with the CISS dataset at the time of extraction. All recorded occupant injuries were classified into anatomical regions prior to analysis. Thoracic injuries included rib fractures, sternal fractures, and thoracic organ injuries; lumbar spine injuries included vertebral fractures and associated soft-tissue injuries; head, abdomen, cervical spine, upper extremity, and lower extremity injuries were grouped using consistent AIS region codes. Multi-injury occupants were assigned a Maximum AIS (MAIS) value. Region-specific AIS2+ and AIS3+ indicators were computed for analysis. All estimates were computed using CISS vehicle- and occupant-level sampling weights. Weighted variance estimation was not performed, as the analysis focused on descriptive injury-pattern characterization rather than inference or population-level uncertainty estimation.

3) Identification of Representative Crash Modes for Testing

Because the objective of the study was to characterize occupant injury mechanisms associated with L-type intersection crashes, the field-data analysis was used only to identify a common crash severity and to quantify injury patterns associated with L-type crashes. These observations motivated the selection of L-type boundary conditions for a controlled crash test, but the boundary conditions were not directly obtained from a specific case in the field data.

B. Controlled L-type Crash Methodology

A controlled full-scale crash test was performed to generate the vehicle-level kinematic environment used for the occupant simulations described in this study. The test configuration was selected to represent the lateral loading conditions characteristic of L-type intersection crashes identified in the field-data analysis, through controlled vehicle trajectories, impact alignment, and pre-defined velocity conditions. To preserve anonymity of the participating organizations, vehicle information is described only in terms of vehicle class and global properties rather than manufacturer or model-specific details.

1) Physical Crash Test Configuration

The physical test involved a left-side impact between a mid-sized sport-utility vehicle (SUV) serving as the struck vehicle (mass approximately 2,000 kg), and a compact SUV serving as the striking vehicle (mass approximately 2,000 kg). Both vehicles were propelled along approximately orthogonal paths representative of an intersection conflict scenario. The striking vehicle contacted the struck vehicle with a full overlap of the driver-side wheel well, diagrammed in Fig. 3. Each vehicle travelled at 40 km/h prior to impact, producing a combined closing speed consistent with moderate-severity side impact conditions. The struck vehicle mass, geometry, and ride height corresponded to a typical compact SUV, while the striking vehicle properties were representative of a mid-sized

SUV. Detailed structural or manufacturer-specific characteristics were not required for the objectives of this study and are therefore not reported.

Two front-row surrogate occupants were installed in the struck SUV. The driver position was occupied by a side-impact ES-2re ATD, and the front-seat passenger position was occupied by a Hybrid-III 50th percentile male ATD. The physical ATDs were positioned according to the National Highway Transportation Safety Administration (NHTSA) protocol outlined in the appendix material of FMVSS208. Instrumentation included standard head centre-of-gravity (CG) accelerometers, neck load cells, thoracic deflection or acceleration sensors depending on surrogate type, pelvis accelerometers, femur load cells, and belt-force. Full channels were available for the passenger Hybrid-III along with seatbelt loading, while the driver data channels were more limited. These channels provided the physical-test reference data for evaluating the occupant compartment finite element model and downstream HBM simulations. The time-history data was augmented by overhead and in-vehicle video of the crash event. Additionally, detailed measurements of ATD seated positions were recorded relative to the nearest front door-striker for use in positioning the simulated occupants in the vehicle environment.

2) Event Timing, Pulse Extraction, and Restraint System Operation

Vehicle-to-vehicle contact, in the physical test, produced an acceleration event lasting approximately 130 ms with an initial impact ΔV of 8.33 m/s (30 km/h). Vehicle-to-vehicle timing was aligned by closing of a circuit when foil strips on each vehicle connected. The crash pulse was recorded at the airbag control unit (ACU) location within the struck vehicle, providing local tri-axial accelerations and rotational-rate time histories required to characterize the vehicle's rigid-body response. These channels were subsequently filtered using an SAE J211 CFC 60 filter prior to use in simulation. As z-axis acceleration and x-y axis rotations were negligible, the pulse was simplified to in-plane accelerations and z-axis rotational velocity, shown in Fig. 2.

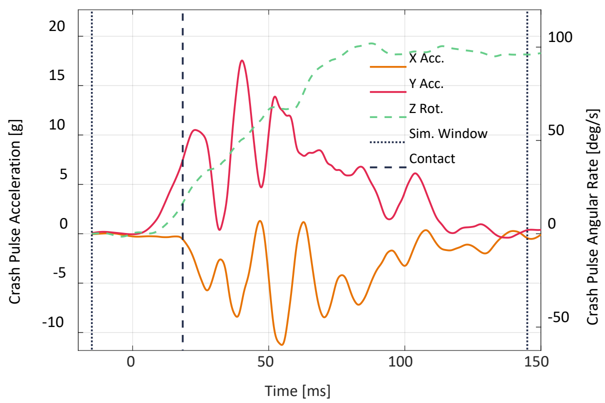

Fig. 2. Filtered L-type Crash Pulse ΔV_{XY}=8.33 [m/s]

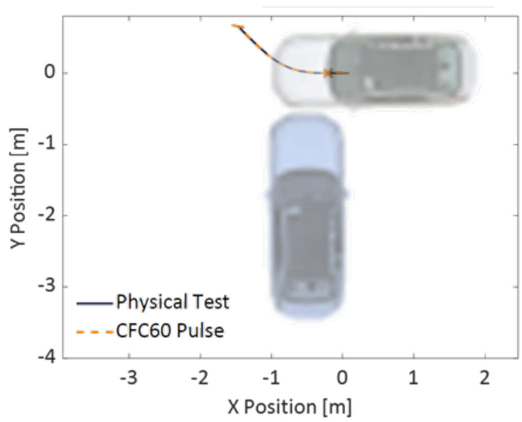

Fig. 3. L-type Crash Diagram

During the physical crash test, the following restraint systems in the struck vehicle deployed:

- driver and passenger curtain airbags
- driver and passenger seat-mounted side airbags
- driver centre side airbag
- driver and passenger belt pretensioners

All systems deployed simultaneously at approximately 12 ms after initial vehicle-to-vehicle contact.

C. LS-Dyna Finite Element Occupant Simulation and Analysis

The finite element simulations described in this study reproduced the physical L-type crash test using two occupant surrogate families: a Hybrid-III 50th percentile male ATD model and a GHBMC v6.0 50th percentile male human body model. All model boundary conditions were derived directly from the physical crash test to ensure that ATD and HBM responses were evaluated under an identical, fully defined loading environment.

1) Occupant Compartment from OEM Vehicle Model

An OEM FEA model of a mid-sized SUV was simplified into a reduced occupant compartment model for computational efficiency. The reduction procedure removed components not expected to influence occupant kinematics (e.g., rear seats, wheels, drivetrain, cargo area) while preserving the frontal seats, door structures, interior trim, instrument panel, centre console, and restraint system mounting points. A floorboard carpet was not included. The resulting compartment model contained approximately 2,700 parts and 3.8 million nodes, retaining the structural detail necessary to capture contact interactions between the occupant and the interior surfaces. The model is set in a right-handed coordinate system defined by global X forward, Y towards the passenger side of the vehicle, and Z downward.

The physical crash test provided the complete kinematic environment, including the 160 ms bi-axial acceleration pulse and z-axis rotational history, restraint firing times, and occupant kinematics used to evaluate model fidelity. The crash pulse was measured at the vehicle's airbag control unit (ACU) and was filtered at SAE CFC 60. A time window of 160 ms, beginning 36 ms prior to first contact, was extracted for simulation use. This ensured that the full lateral loading event and associated rotational components were captured while avoiding unsupported assumptions regarding pre-impact motion. The filtered pulse was applied at the ACU location in the finite element model, consistent with the coordinate system defined in the reduced compartment model and maintaining the inertial properties of the full un-modified OEM mid-sized SUV model. OEM provided models were employed for the restraint systems active in the crash test for both driver and passenger including curtain airbags (CAB), outboard in-seat side airbags (SAB), and 2-D 3-point seatbelts with active pretensioners. Airbag and seatbelt pre-tensioners fired simultaneously at 12 ms after contact in both the physical crash testing and FEA simulations for both driver and passenger. These activation times were applied uniformly in the ATD and HBM simulations to ensure that surrogate differences did not arise from differences in restraint triggering. Simulated airbags were only deployed if they both activated in the physical crash test and contacted one of the occupants.

2) Occupant Surrogate Models

Hybrid-III 50th percentile male ATD models were used in the driver and passenger positions for baseline ATD simulations, as well as Global Human Body Models Consortium (GHBMC) v6.0 50th percentile male human body models were employed to compare injury patterns and risk predictions against the field data. Each surrogate was positioned to match the physical test occupant seating positions, prioritizing H-point, pelvis angle, head CG location, and knee spacing data recorded in physical test documentation relative to the door striker on each side of the vehicle. This results in the driver positioned with right foot on accelerator and both hands on the wheel at 10 and 2 o'clock. The passenger was posted in a standard, legs parted, posture with arms just above the thighs. Once positioned, OASYS Primer was used to perform quasi-static seat cushion deformation around the Hybrid-III ATD prior to simulation. Matched positioning was achieved for the GHBMC by first visually aligning the skeletal structure with the ATD model frame to coordinate postures and confirmed against physical test ATD positioning measurements. Subsequently the GHBMC H-point in-seat was matched through settling pre-simulation using standard spring-pull positioning simulations with temporarily rigidized skeletal structure. The GHBMC with rigidized skeleton was translated above the seat and driven into position using a minimum-impulse prescribed motion, to obtain settled models with deformed HBM flesh and seat cushions for both driver and passenger. Both ATD and GHBMC occupant models were constrained during the crash simulations through standard LS-Dyna contacts with interior surfaces, seat cushions, and restraint systems.

3) Physical and Simulation Occupant Injury Prediction Metrics

Injury prediction for physical and simulation occupants was performed through Injury Risk Functions (IRFs) from the literature that present the percentage risks of injury for specific body regions in terms of injury severity by AIS level potentially from 1 to 6. Risk of Traumatic Brain Injury (TBI) was assessed, at an AIS2+ level, with the DAMAGE [16] metric which acts as an estimation of strain in brain tissue under rotational acceleration about the head centre of gravity. AIS2+ and AIS3+ skull fracture risk was assessed with the Head Injury Criterion (HIC) [17]as a function of head linear acceleration. Injury risk to the cervical spine, for AIS2+ and AIS3+, were estimated with the Nij [17] IRF based on tension-compression axial forces and flexion-extension moments in the upper neck. Thoracic injury was estimated by multiple methods to accommodate the mixed frontal and lateral loading of the crash scenario and the variations between Hybrid III ATD and HBM. The Hybrid III ATD assesses thoracic injury with a single point anterior-posterior deflection metric (Dmax) [18] suitable for frontal loading conditions, while the HBM allows for more varied assessments using the multi-point maximum deflection (Rmax) and PCA [19], and half-lateral normalized deflection [20] for AIS3+ risks under frontal and lateral loading respectively. Risk of injuries to the pelvis and left and right lower extremities were estimated using the Knee-Thigh-HIP (KTH) index [21] for pelvis and femur fracture based on femoral axial forces, and the Revised Tibia Index (RTI) [22] for tibia fracture based on forces and moments in the lower leg. This selection of IRFs were chosen based on the injury patterns identified in the field-data analysis and the correspondence between ATD instrumentation and analogous quantities available in the GHBMC HBM.

4) Acceleration Pulse Scaling

Once the vehicle environment with ATD models was evaluated against the baseline crash pulse and shown to agree with the physical crash-test response in terms of kinematic trends and signal timing, the crash pulse was then scaled to allow additional investigation at a more severe crash condition, approximating a collision between similar vehicles each traveling at 70 km/h. Pulse severity is often characterized by integration of the acceleration pulse with time, resulting in a change in velocity ΔV. A constant scale factor, C, was applied to ΔV, which is equivalent to a constant scale factor applied to the acceleration curve, a(t), Equation (1).

As scaling of translational acceleration is proportional to scaling of ΔV, it was assumed that the struck vehicle ΔV components are linearly proportional to the combined initial velocity of both vehicles. This translational scaling assumption also resulted in a corresponding linear scaling of angular velocity, under the additional assumptions that the striking vehicle moved with the struck vehicle, the moment arm between the vehicles' centres of gravity remained approximately constant, and the struck vehicle deformed without fragmenting. While the physical vehicle did not experience occupant compartment intrusion in the baseline crash event, such deformation may occur at higher severities. This scaling approach preserved overall kinematic trends but did not capture potential nonlinear structural deformation or intrusion effects at increased severity.

Fig. 4 shows a simplified vehicle with a force applied to the front driver's side wheel well. The angular momentum equation of motion for this simplified vehicle is represented by Equation (2), where L_x is moment arm along vehicle length from impact point to vehicle centre of mass, I_{zz} is the moment of inertia of the vehicle in plane about its centre of mass, m is the vehicle mass, and a(t) is the linear acceleration pulse. Constant angular velocity, $\dot{\theta}$, was found directly proportional to ΔV, Equation (3), with the previous assumptions ensuring that the mass, moment of inertia, and moment arm length remained approximately constant with time. The assumptions were tested by applying a linear fit to angular rate against ΔV, Fig. 5, which showed 89% of the variation in angular rate about the mean being explained by a constant coefficient on ΔV.

$$C \cdot \Delta V = C \cdot \int_{t0}^{t1} a(t)dt \,, \qquad (1)$$

$$I_{zz}\ddot{\theta} = L_x m a(t) = \frac{L_x}{I_{zz}} m a(t) \,, \qquad (2)$$

$$\dot{\theta} = \frac{L_x}{I_{zz}} m \int_{t0}^{t1} a(t)dt = \frac{L_x}{I_{zz}} m \Delta V(t) \,, \qquad (3)$$

A 1.75 scaling factor for the severe crash case was selected increasing from 40 km/h to 70 km/h initial velocities for both struck and striking vehicles, or a ΔV of 52.5 km/h with crash energy tripled. The OEM FEA model of the occupant compartment was then simulated with both driver and passenger occupants for dummy and HBM models at both nominal and severe crash acceleration pulses. The LS-Dyna outputs for nodal acceleration and location history and cross-section force and moment history were then processed and fed into the various injury risk prediction metrics detailed above for all 4 simulation cases.

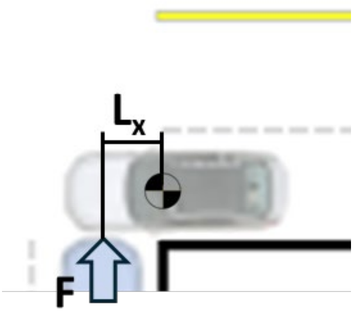

Fig. 4. Angular Momentum Free-Body Diagram of a Vehicle

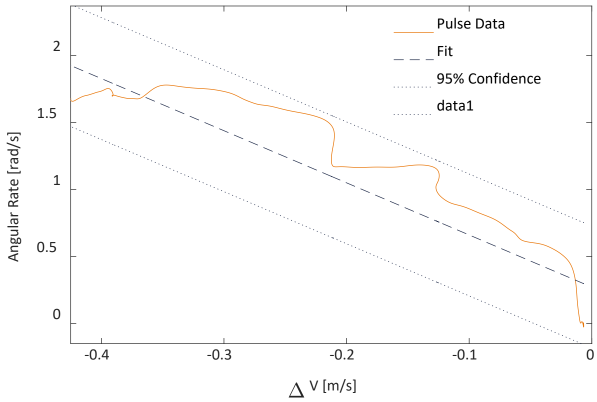

Fig. 5. Pulse Scaling Assumption Check, Equation (3)

III. RESULTS

A. Field Data Analysis

Over the specified period, 16 million crashes (N=17,463 unweighted) are represented in CISS with 28.8 million (N=34,873 unweighted) occupants injured. Application of the selection criteria to the CISS dataset identified 1,772 unweighted occupants in intersection-related side-struck crashes, corresponding to an estimated 1,238,112 occupants using CISS sampling weights. Within this cohort, L-type side impacts accounted for 21.2% of unweighted cases and 18.0% of the weighted occupant population, representing approximately 5% of all towed-vehicle crashes and 7% of all intersection crashes in the weighted dataset. Pure T-type crashes, from zone P, Fig. 1, accounted for 8.7% of unweighted and 7.4% of weighted intersection and side-struck cases; while zone Y of the CDC diagram in Fig. 1 was most commonly observed, containing crashes overlapping between L- and T-type, with 33.4% of unweighted, and 28.9% of weighted cases. Table A1, in the Appendix, shows the distribution of occupant height associated with L-type crashes using the CISS data. Occupant height was summarized for male, female, and combined male–female groups, with the 50th percentile male Hybrid III ATD corresponding closely to the median male height.

Across the L-type cases, the analysis identified 53,825 AIS2+ injuries, composed of 30,504 AIS2 and 22,325 AIS3+ injuries. L-type crashes contained the highest frequency of AIS3+ injuries when compared to other side-struck intersection crashes, though together L- and T-type crashes exhibited the most frequent injury occurrence overall. Thoracic and lumbar spine injuries dominated the serious and moderate injury burden. Thoracic injuries represented 60.2% of AIS2+ cases (n = 32,400) and 45.3% of AIS3+ cases (n = 10,559), while lumbar spine injuries represented 18.8% of AIS2+ injuries (n = 10,106) and 42.0% of AIS3+ injuries (n = 9,800). Head injuries accounted for 4.7% of AIS2+ and 2.6% of AIS3+ outcomes, and all remaining injury regions each contributed less than 5% of AIS2+ or AIS3+ injuries. At higher severity (AIS4+), injuries were concentrated in the abdominal region (81.8%) and head region (18.2%), although these cases were rare compared to the AIS2+ and AIS3+ thoracic and lumbar injuries that defined the modal injury patterns in L-type impacts. Comparison with T-type intersection crashes demonstrated that L-type crashes were associated with a greater probability of thoracic and lumbar AIS2+ and AIS3+ injury, whereas T-type crashes showed higher frequencies of head and abdominal AIS2+ injuries. These distinctions were consistent across weighted distributions and reflect fundamentally different loading environments for L-type and T-type events.

To further contextualize the selected vehicle representation and impact severity, vehicle-type distributions and associated injury outcomes for L-type crashes were also examined. Detailed breakdowns are provided in Tables A2-A5 and Figure A1 in the Appendix. These data show that, while multiple vehicle classes were represented in the dataset, systematic differences in injury probability with ΔV were observed across vehicle types, with lower-profile vehicles generally exhibiting higher injury risk at a given ΔV compared to SUVs. Accordingly, the selected SUV-based simulation conditions, including the baseline (ΔV = 30 km/h) and scaled (ΔV = 52.5 km/h) cases, were interpreted as representing moderate and higher severity regimes where injury risk increases more gradually than sedan crashes.

B. Physical Test Outcomes

As discussed above with the simulation crash pulse description, the physical test resulted in an initial contact between striking and struck vehicles of 130 ms and a ΔV of 30 km/h. The driver physical ATD had few signals recorded, only head kinematics, while the passenger physical ATD's head, pelvis, and chest CG kinematics were recorded. Additionally in the passenger ATD the belt forces were recorded for lap and shoulder belt sections along with upper neck forces and moments and femoral forces. Time histories of these signals are shown in Appendix Figs. A2-A7. Front facing video was recorded in the occupant compartment to capture ATD motion and allow confirmation of active restraint system trigger timing. The driver ATD moves left into the curtain and side airbags, while the passenger ATD extends over the central console and experiences minimal engagement with the passenger side restraints. The passenger ATD does not extend far enough to encounter the driver ATD or the driver centre seat airbag.

C. FE Simulation Outcomes

1) Reproduction of the Physical L-Type Crash Test ATD Responses

Visual evaluation of test video showed qualitative verification of simulation fidelity when compared with simulation videos framed to a similar perspective. Both the ATD and HBM simulations exhibited visible displacement of the central console towards the driver under loading from the passenger. A set of selected time-history comparisons, illustrating kinematics and loading, between the physical test, ATD simulations, and HBM simulations are included in the Appendix, for both driver and passenger, demonstrating that the simulation environment reproduced the crash-test kinematics successfully, Figs. A2-A19. Not all physical ATD instrumentation produced a recorded signal due to limitations of the onboard DAS. Appendix Table A6 provides CORA [23] and ISO/TS 18571:2024 [24] cross-correlation metrics for each Hybrid III ATD signal recorded in both physical and simulation testing, where values from 0.4 to 0.6 are fair, 0.6 to 0.8 are good and greater than 0.8 are considered excellent. The resultant acceleration signals for both passenger and driver show excellent CORA scores along with the neck anterior-posterior shear force and belt forces. The remaining neck forces show good correlation along with most of the acceleration direction components while the neck flexion-extension moment and left femur force show moderate to poor correlation. Slope and phase metrics of the ISO/TS 18571:2024 correlation follow similar trends, while the magnitude metric remains low for all signals. Despite high CORA scores, simulation seat belt forces peaked higher than physical test data with 35% difference in lap belt and 45% difference in shoulder belt loading. Similar differences were observed in axial femur forces with the simulated ATD experiencing more than double the loading. All resultant accelerations for both driver and passenger showed less than 11% difference in peak magnitudes. Overall, the majority of signals demonstrated good correlation in timing and phase, with larger discrepancies observed in peak magnitudes for belt and femur loads. These validated kinematic responses provided the basis for comparing ATD and HBM behaviour and injury metrics.

2) Simulated ATD vs HBM response

The GHBMC HBM skeletal detail and instrumentation provided internal deformation data not available from ATDs. Kinematically the head, thoracic, and pelvis tracked locations are consistent both between occupant model types and with the kinematics observed in the crash test. The simulation accelerations of pelvis and chest are more closely aligned with test data than the head accelerations for the HBMs due to increased neck flexibility relative to ATDs. The HBM also experiences greater measured thoracic displacement than the modelled ATD, but similar kinematics in the neck, lumbar spine and lower extremities, Figs. A1-A4. Overall, the GHBMC occupants exhibited consistent kinematic trajectories to the ATD occupants.

Figs. 6 and 7 illustrate the peak lateral excursion of simulated occupants relative to initial position and the differences in anthropometry between the two nominally 50th male surrogates. In both the baseline and high severity crash pulse, the postures, and positions of the ATD models and HBMs and the peak excursions are matched. The peaks in lateral displacement from initial position for the baseline crash pulse happen earlier for the ATD driver at 103 ms than the HBM driver, 114 ms, while the passenger timing is more similar at 143 and 142 ms for ATD and HBM models. The high severity crash pulse, Fig. 7, does result in increased discrepancies between the kinematics of occupant types, primarily in the lateral flexibility of the spine, for both driver and passenger, and rebound behaviour of the driver. The peak lateral displacements of Fig. 7 occur with a similar pattern, earlier for ATD driver, 94 ms, than HBM driver, 100 ms, and later for the ATD passenger, 158 ms, compared to 139 ms for the HBM. Fig. 8 shows the L-type crash event over time, recalling that the impact occurs at 12ms and restraints systems fire at 33 ms. At 90 ms the differences between ATD and HBM model responses are minimal, but the passenger HBM (Red) began to slide out from under the shoulder belt. At 120 ms the passenger HBM's torso is fully extended over the centre console while the driver HBM has experienced greater thoracic loading into the CAB and SAB. The ATD model had a comparatively stiff spine and thorax, experiencing less leaning for the passenger and equivalent driver loading into the side airbags and door. After the peak lateral motion of the driver, the HBM rebounds with more spinal curvature. The observed differences in timing and spinal flexibility contributed to variations in thoracic loading and restraint interactions observed in the predicted injury outcomes.

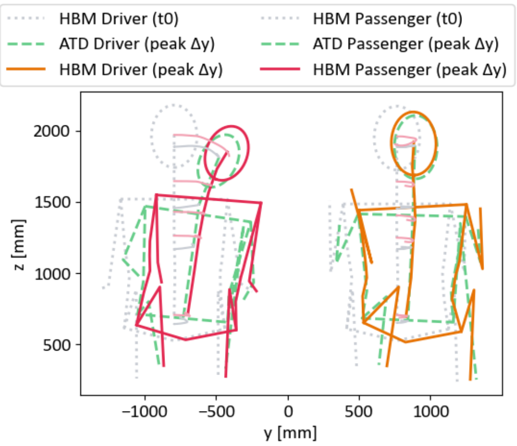

Fig. 6. Frontal View Lateral Excursion Kinematics for Baseline Pulse Simulations: Driver (Right) and Passenger (Left)

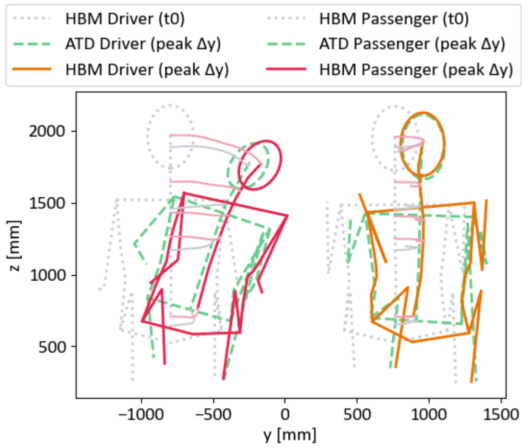

Fig. 7. View Lateral Excursion Kinematics for High Severity Pulse Simulations: Driver (Right) and Passenger (Left)

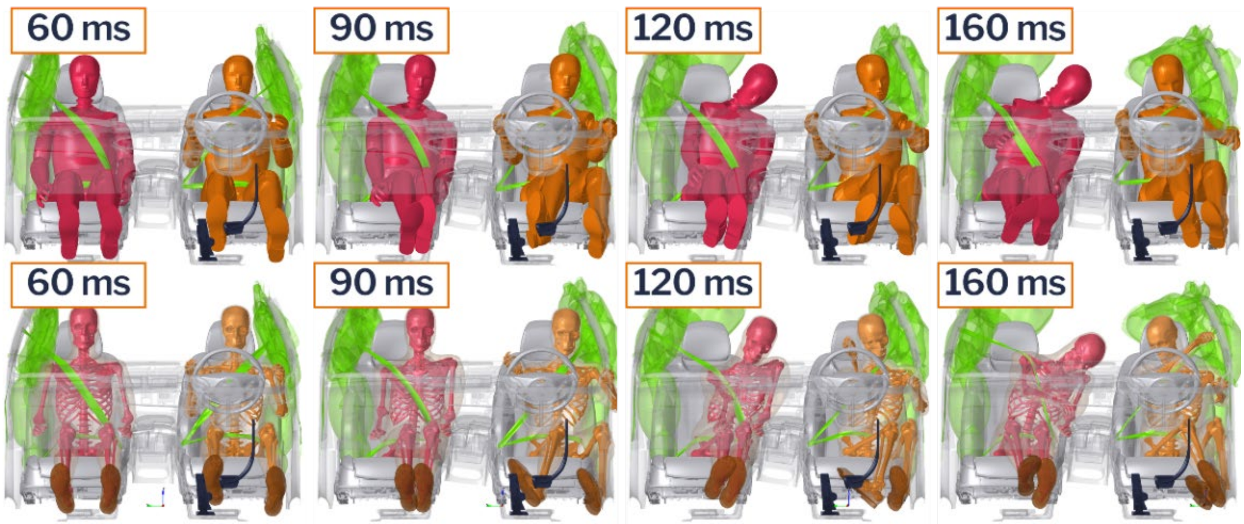

Fig. 8. Frontal View Time History Visualization of Baseline Simulation (ΔV=30 km/h)
ATD (Top) vs HBM (Bottom); Driver (Orange) and Passenger (Red) with Restraints (Green).

Fig. 9 shows a comparison of L-type crash pulse severity between the nominal event of ΔV=30 km/h and a scaled bi-axial and rotational pulse to a ΔV=52.5 km/h event. At 90 ms the high-severity pulse HBM posture resembled the 120 ms posture of the baseline severity pulse, showing temporal compression of the loading event. Recalling that the increased severity event is equivalent to the two vehicles both traveling at 70 km/h just prior to contact, the time history data in the Appendix shows an expected increase in most metrics.

The injury patterns predicted for both driver and passenger simulated occupants exhibited a range of severity and risk dependent on the occupant model and acceleration pulse ΔV, despite similar kinematics. However, occupant injury risk predictions were low for most body regions. The highest baseline pulse predicted risk was observed for the HBM passenger with a 71% risk AIS3+ thoracic injury predicted by the multi-point maximum deflection metric. Other injury predictions remained below 12% AIS3+ risk for both passenger and driver for the

30 km/h ΔV crash event, with 11.3% risk from single point chest deflection to the driver HBM and about 5% risk from Nij for all surrogates and vehicle positions. On the AIS2+ level, both simulated surrogates for the passenger and the HBM driver were predicted to receive lower extremity injuries to the tibia at 100% risk, while KTH predicted negligible injury risk to the pelvis/thigh. Remaining AIS2+ injury predictions remained below 5% for the reconstructed crash test, except Nij predicting the second highest risk at approximately 13% for both passenger and driver and both surrogate models. The AIS2+ and AIS3+ injury risk predictions are recorded below in Table 1 and respectively for both baseline and high pulse severity. Risks greater than 10% have been bolded, as was the high severity pulse ΔV, while the ATD model injury predictions have been shaded.

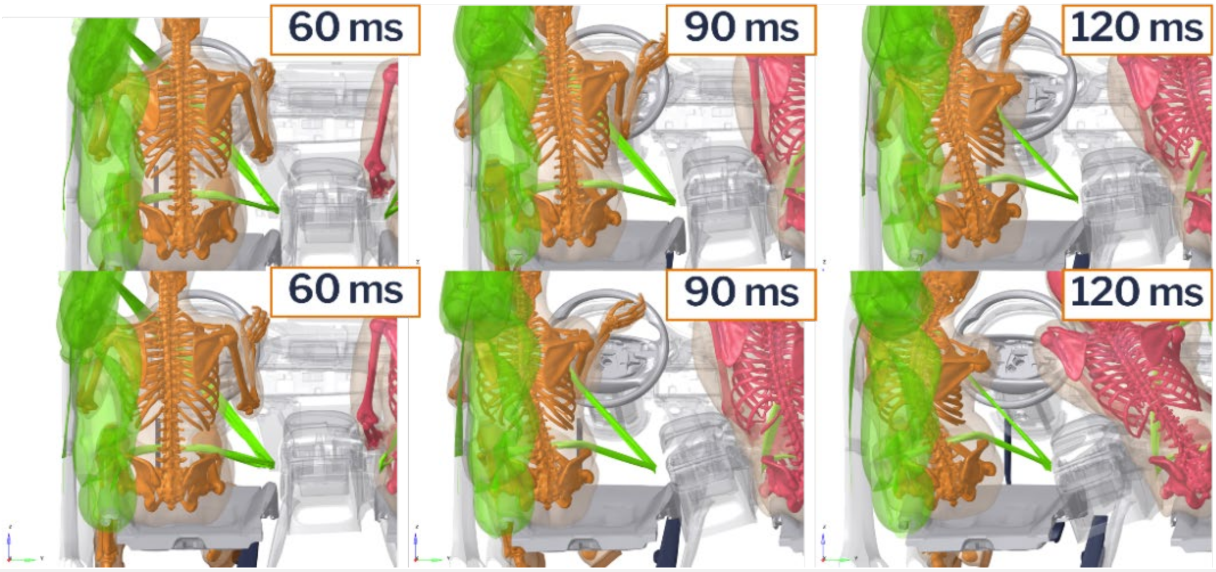

Fig. 9. Rear View Time History Comparison of Simulation Severity for the HBM Driver, ΔV=30 km/h (Top) and ΔV=52.5 km/h (Bottom);
Driver (Orange) and Passenger (Red) with Restraints (Green).

TABLE 1
AIS2+ INJURY RISK PREDICTIONS FROM SIMULATIONS

	Position	Driver				Passenger			
	Surrogate	ATD	HBM	ATD	HBM	ATD	HBM	ATD	HBM
	Crash Event ΔV	30.0	30.0	**52.5**	**52.5**	30.0	30.0	**52.5**	**52.5**
Brain	DAMAGE	0.8%	7.5%	26.1%	40.5%	1.9%	1.5%	1.5%	0.9%
Head	HIC15	0.1%	0.2%	**12.8%**	**12.0%**	0.0%	0.0%	1.7%	3.5%
Neck	Nij	**13.2%**	**13.3%**	**15.6%**	**14.1%**	**13.2%**	**13.8%**	**14.3%**	**17.6%**
Pelvis/Knee	KTH_L	0.6%	0.4%	0.5%	0.4%	0.5%	0.4%	0.6%	0.4%
	KTH_R	0.6%	0.4%	0.7%	0.5%	0.8%	0.7%	1.1%	0.9%
Lower Ext.	RTI_L	0.0%	0.0%	0.0%	0.0%	0.0%	0.0%	0.0%	0.0%
	RTI_R	4.2%	**99.9%**	16.3%	**99.9%**	**99.9%**	**99.9%**	**99.9%**	**99.9%**

3) Injury Metric Sensitivity to Increased Pulse Severity

Head injury metrics (HIC15 and DAMAGE) increased modestly with scaling, while neck loads (Nij) exhibited greater sensitivity to increased lateral occupant excursion and belt loading. Thoracic injury metrics demonstrated the most pronounced surrogate-dependent divergence. Hybrid-III ATD chest deflection increased with severity but remained limited by the ATD's single-point thoracic sensor architecture. In contrast, the HBMs experienced increases in thoracic deformation injury predictions within the various metrics and with higher severity pulse, consistent with switching from single point to multi-point assessment in a primarily lateral loading condition. The passenger HBM, who experienced slipping from under their belt and experienced excursion over the central consol, saturated the multi-point risk metrics for AIS3+ risk at higher severities. The differences in HBM chest deflection and torso kinematics are shown in Fig. 9.

TABLE 2
AIS3+ INJURY RISK PREDICTIONS FROM SIMULATIONS

	Position	Driver				Passenger			
	Surrogate	ATD	HBM	ATD	HBM	ATD	HBM	ATD	HBM
	Crash Event ΔV	30.0	30.0	**52.5**	**52.5**	30.0	30.0	**52.5**	**52.5**
Head	HIC15	0.1%	0.1%	4.2%	4.0%	0.0%	0.0%	0.6%	1.3%
Neck	Nij	5.0%	5.1%	6.7%	5.6%	5.0%	5.4%	5.8%	8.5%
Thorax	Dmax	0.1%	**11.3%**	0.1%	**20.1%**	0.4%	8.5%	0.6%	**11.4%**
	Rmax	-	**59.4%**	-	**88.5%**	-	**71.3%**	-	**99.9%**
	PCA	-	**42.9%**	-	**74.8%**	-	**59.4%**	-	**99.9%**
	Lat. Impact	-	**38.4%**	-	**71.9%**	-	**51.3%**	-	**98.3%**
Pelvis/Knee	KTH_L	1.0%	0.8%	0.9%	0.8%	0.9%	0.8%	1.0%	0.8%
	KTH_R	1.0%	0.9%	1.2%	0.9%	1.2%	1.2%	1.6%	1.4%

IV. DISCUSSION

A. *Field Data Evaluation*

L-type collisions represented 18% of side impacts in intersections and approximately 7% of all intersection crashes in the weighted CISS dataset, with an additional 30% of potential L-type cases classified in the adjacent "Y" damage zone, of Fig. 1, if an L-type crash causes damage overlap with T-type zone "P." Although both L- and T-type events were lateral impacts, the off-centre loading characteristic of L-type collisions introduced substantial rotational motion that produced distinct occupant response patterns and injury distributions. Thoracic and lumbar spine injuries were the dominant AIS2+ and AIS3+ outcomes, with low contributions from head and abdominal regions. These findings were consistent with historical observations that thoracic injuries have constituted approximately 40% of AIS3+ and 53% of AIS2+ injuries in side-impact events [25]. The specific injury mechanisms and injury occurrence ratios of L-type crashes in the field data motivated the use of a controlled L-type crash test to evaluate Hybrid-III ATDs and GHBMC v6.0 HBMs within a well-defined lateral and rotational loading environment.

B. *Occupant Kinematic and Loading Variation Across Physical Test and Simulations*

The occupant response simulations, for pairs of Hybrid-III ATDs and GHBMC v6.0 HBMs, captured the principal kinematic characteristics observed in the physical L-type side-impact crash test. Occupant acceleration time histories agreed substantially in both timing and magnitude between the test and both simulations. Test video and simulation renderings showed consistent torso excursion and belt-engagement behaviour. The average of CORA [23] and ISO/TS 18571:2024 [24] cross-correlation metrics showed good correlation for driver and passenger occupants. The reduced score for magnitude in the ISO evaluation can be attributed to localized L1 error after the DTW alignment [24,26], which can over penalize noise with narrow but high peak values. Internal deformation responses in the HBM followed the timing of external motion, and larger discrepancies between the ATD and HBM were primarily in head and pelvis rotation as well as force and moment loading in the neck and lower extremities. The rotational rate differences are explained through comparison of the ATD's rigid cylindrical joints against HBM ball-in socket joints and greater spinal flexibility. Loading can be similarly related to model flexibility providing different impact angles, or simply due to alternative load paths in the HBM. The ATD's single-point thoracic linear actuator may not be sufficient to represent complex deformation patterns, such as lateral loading from the centre consol or the door trim.

C. *Occupant Injury Prediction*

The differences in injury-metric response can be grouped into three categories. First, surrogate-dependent outcomes arose when ATD and HBM sensing or anatomical fidelity differed, such as in thoracic deformation where the HBM captured multi-point rib loading absent in the ATD instrumentation. Second, seating-position-dependent outcomes appeared where the driver and front passenger occupants experienced distinct geometric constraints, including the driver's outboard loading into the SAB, CAB, and door and the passenger's medial excursion over the centre console. Third, condition-dependent outcomes were associated with changes in ΔV, where the increased pulse severity produced greater excursion and internal loading for both occupants but with nonlinear scaling due to restraint timing, geometry, and interior interaction.

Driver and passenger kinematic differences were more pronounced than those between surrogates. The driver response is dominated by inertia, translated toward the struck-side interior panels and engaged with the in-seat side airbag, curtain airbag, and door. Thoracic skeletal loading resulted from this interaction, while driver spinal curvature and rib deformation increased visibly with crash severity, shown in Figs. 6-7 and Fig. 9. For the magnified ΔV simulations, no adjustments were made to airbag trigger timing; airbags still deployed at 12 ms after contact, resulting in closer proximity of the driver torso to the deploying side thoracic airbags. In L-type loading, where occupant translation toward the struck-side structure is accompanied by rotation, the fixed deployment timing of these simulations may not coincide with the optimal occupant position for side-airbag engagement. Depending on impact severity and rotation rate, the side airbag may deploy after or during occupant contact with the door surfaces, potentially reducing effective energy absorption or altering loading pathways [14,27]. By contrast, the passenger avoided engagement with both the in-seat side-airbag and the curtain airbag for both simulation pulse severities. Large medial excursion carried the passenger's upper body over the centre console while the lap belt and lower-extremity contact constrained the pelvis. The shoulder belt did not engage due to its orientation relative to vehicle acceleration. The torso folding produced higher thoracic injury risk for the passenger than the driver, which aligned with far-side injury mechanisms reported previously [2,28–31]. Airbag deployment and trigger timing in L-type crashes should consider the loading direction and occupant position for ideal deployment. The AIS3+ risk values, Table 2, exceeded the 38% rib-fracture probability reported for SAFER in Mroz et al. [16], although the study designs and surrogate characteristics differed and no direct comparison can be made.

Prior studies suggest that side-airbag deployment in real-world lateral crashes is sensitive to impact location, sensor coverage, and loading direction, with documented cases of delayed or absent deployment when impacts occur outside nominal sensing zones or under crash geometries outside nominal sensing regions[13,14]. In L-type crashes, the forward-offset contact location and induced yaw motion may increase the likelihood of delayed side-airbag deployment or deployment after significant occupant lean toward the door has already occurred. Such delays may reduce protection against door trim and armrest interaction or lead to airbag inflation while the torso is already supported by interior structures, with implications for thoracic injury risk [27,32]. The results of the increased severity simulations, along with existing studies, indicate that side-airbag triggering and deployment strategies for L-type crashes should account not only for lateral acceleration magnitude but also for rotational kinematics and occupant translation relative to the struck-side interior. Algorithms developed primarily for perpendicular T-type impacts may therefore require adaptation to accommodate the coupled lateral-rotational motion and posture evolution characteristic of L-type events [14,15,27].

Lower-extremity kinematics involved multiple impacts to interior surfaces. The driver's outboard leg impacted the door, and the inboard leg contacted the pedal assembly prior to following the other leg. The inboard foot caught on the brake pedal, producing the ankle deformation visible in Fig. 8 at 90 ms. This response occurred in both surrogates under both acceleration severities but was more pronounced with the HBM due to greater joint flexibility. Passenger lower extremities struck the centre console and contralateral leg and produced equal or greater RTI values despite the absence of a pedal contact. The discrepancy between simulated and field-data lower-extremity injury risk therefore likely reflected two interacting factors. First, rigidized pedal support structures and simplification of the interior geometry concentrated loads in ways that may not occur in production vehicles. Second, inertial rotation of the legs and subsequent interaction with interior structures were consistent with known side-impact injury mechanisms [33–35]. The simulations reproduced reasonable loading modes but possibly overpredicted the severity of localized lower-extremity loading due to peculiarities of the specific simulation environment.

D. Limitations

Interpretation of the simulation outcomes must consider physical and conceptual limitations. The analysis relied on a single controlled crash test and its simulated reproduction, which limited the ability to generalize across alternative vehicle geometries, occupant postures, and impact configurations. Only one impact severity was recorded, and two were simulated, limiting the estimation of how steeply injury risk increases with crash ΔV. Additionally, scaling of the bi-axial and rotational crash pulse to increase impact severity was limited to approximating the potential true high severity crash pulse. Other motion such as z-axial linear acceleration and out of plane rotations were negligible, but not absent and may become more significant with increasing severity or variations in vehicle geometry and mass distribution.

This study was limited to a 50th percentile male anthropometry, and variations in occupant size and sex may influence the observed response. Future work should extend the analysis to female and other anthropometric representations. The Hybrid-III injury-risk functions available for ATD outputs were developed primarily from frontal loading conditions, and the multi-point thoracic functions used for the HBM were developed from PMHS datasets for use with the THOR ATD. Application of these functions in the mixed offset-lateral and rotational loading of an L-type environment should therefore be interpreted cautiously. Lumbar force and moment loads were not recorded for the physical Hybrid III ATD, but was collected for both simulated occupants. While the simulated lumbar loading could be measured, there is no injury metric available for lateral loading of the lumbar region. Future work to investigate the effect of combined lateral and rotational acceleration on lumbar loading. Some discussed injury mechanisms were identified through kinematic visualization because corresponding physical-test force channels were unavailable. Simplifications in the reduced occupant-compartment model, including rigidized pedal supports and idealized centre console surfaces, may also have influenced the simulated loading pathways, particularly in the lower extremities. Reduction of the model by removal of non-occupant-contacting components, may have compromised the anchoring of the centre console allowing increased passenger excursion.

V. CONCLUSION

The present study combined field-data analysis, a controlled L-type intersection crash test, and paired ATD-HBM finite-element simulations to investigate occupant kinematics and injury-risk sensitivity under lateral loading conditions representative of high-injury-burden intersection crashes. The L-type intersection crash examined in this study produced significant predicted risks of thoracic and lower-extremity AIS3+ injury for both the Hybrid-III ATD and the GHBMC HBM at baseline severity, and substantially increased thoracic and brain injury risk at higher ΔV. Head and neck injury risks at baseline severity were low to moderate for both surrogates, which was consistent with the relatively low incidence of head AIS3+ injury in the L-type cases identified in the CISS dataset. At higher severity, the driver showed an elevated risk of brain injury using the DAMAGE metric and moderate risk of head impact injury using HIC15. Passenger head-injury risk did not exhibit a similar increase, reflecting the absence of a discrete head contact surface during peak torso excursion.

The simulations demonstrated that the Hybrid-III ATD underrepresented lateral thoracic deformation due to its single-point measurement capability, while the GHBMC HBM resolved multi-point rib deformation patterns that aligned with thoracic injury mechanisms found in L-type field data. In the field-data analysis, L-type crashes accounted for the largest AIS3+ injury burden among the intersection-related lateral impacts studied, exceeding T-type PDOFs. Current regulatory testing protocols most directly evaluate centred planar lateral impacts and may not fully represent the off-centre lateral and rotational combined loading characteristics observed in L-type crashes. In addition to altering occupant kinematics, such rotational lateral loading may also influence the relative timing between occupant motion and the deployment of side-impact restraint systems, reinforcing the importance of evaluating restraint performance under crash conditions that deviate from centred planar loading. The elevated thoracic and lower-extremity injury burden observed in L-type crashes, together with the distinct kinematic responses identified here, suggests that future injury-assessment and restraint-system evaluations would benefit from explicit consideration of rotationally influenced lateral impact conditions. Increasing implementation of automated emergency braking systems and partially automated driving features may alter crash geometries and increase the prevalence of off-centre or oblique impact configurations, reinforcing the need to evaluate occupant protection in L-type crash modes.

VI. ACKNOWLEDGEMENTS

The authors acknowledge the financial and technical support of the faculty, students, and staff of the Center for Applied Biomechanics at the University of Virginia’s Mechanical and Aerospace Engineering Department. Additionally, the work would not have been possible without the support of our OEM partner and associated testing facilities.

VII. REFERENCES

1. Garelli, F., "Side impact crash studied with FE simulation and Human Body Model," Doctoral dissertation, Politecnico di Torino, Turin, Italy, 2021.

2. Gierczycka, D. and Cronin, D.S., "Occupant thorax response variations due to arm position and restraint systems in side impact crash scenarios," *Accid. Anal. Prev.* 106:173–180, 2017, doi:10.1016/J.AAP.2017.05.017.

3. Yoganandan, N., Nahum, A.M., and Melvin, J.W., eds., "Accidental Injury: Biomechanics and Prevention," 3rd ed., Springer New York, ISBN 978-1-4939-1731-0, 2015, doi:10.1007/978-1-4939-1732-7.

4. Zhang, C., Li, X., Lei, Y., Zhang, D., and Zhang, T., "Driver Injury During Automatic Emergency Steering in Vehicle–Vehicle Side-Impact Collisions," *IEEE Access* 12:9400–9417, 2024, doi:10.1109/ACCESS.2024.3353198.

5. Chipman, M.L., Lebovic, G., Desapriya, E., and Gane, J., "Lateral damage and point of impact in intersection crashes: Implications for injury," *Assur. Gest. Risques* 73(4):429–442, 2006, doi:10.7202/1106605ar.

6. Isaksson-Hellman, I. and Lindman, M., "Evaluation of the crash mitigation effect of low-speed automated emergency braking systems based on insurance claims data," *Traffic Inj. Prev.* 17:42–47, 2016, doi:10.1080/15389588.2016.1186802.

7. Cicchino, J.B., "Effectiveness of forward collision warning and autonomous emergency braking systems in reducing front-to-rear crash rates," *Accid. Anal. Prev.* 99:142–152, 2017, doi:10.1016/J.AAP.2016.11.009.

8. Cicchino, J.B. and Zuby, D.S., "Characteristics of rear-end crashes involving passenger vehicles with automatic emergency braking," *Traffic Inj. Prev.* 20(sup1):S112–S118, 2019, doi:10.1080/15389588.2019.1576172.

9. Leledakis, A., Lindman, M., Östh, J., Wågström, L., Davidsson, J., and Jakobsson, L., "A method for predicting crash configurations using counterfactual simulations and real-world data," *Accid. Anal. Prev.* 150:105932, 2021, doi:10.1016/J.AAP.2020.105932.

10. Höschele, P., Smit, S., Tomasch, E., Östling, M., Mroz, K., and Klug, C., "Generic Crash Pulses Representing Future Accident Scenarios of Highly Automated Vehicles," *SAE Int. J. Transp. Saf.* 10(2), 2022, doi:10.4271/09-10-02-0010.

11. Leledakis, A., Östh, J., Davidsson, J., and Jakobsson, L., "The influence of car passengers' sitting postures in intersection crashes," *Accid. Anal. Prev.* 157:106170, 2021, doi:10.1016/J.AAP.2021.106170.

12. Mroz, K., Östling, M., Klug, C., and Höschele, P., "Supplementing future occupant safety assessments with severe intersection crashes selected using the SAFER human body model," *SAE Int. J. Transp. Saf.* 10(2):211–234, 2022.

13. Aldaghlas, T.A., Burke, C., Jenkins, J., Brown, L.J., and Rizzo, A., "Side-Impact Air Bags in Side Crashes: Not Deploying as Designed? A Review of Real World Crash Data," *SAE 2010 World Congress & Exhibition*, SAE Technical Paper, 2010.

14. Bolte, J. and Weisenberger, J., "Bioinjury Implications of Pre-crash Safety Modeling and Intervention Investigators," Final Report for Ohio State University Grant No. DTRT13-G-UTC47, US Department of Transportation (USDOT), Crash Imminent Safety University Transportation Center (CrIS), 2018.

15. Pal, C., Narahari, S., Vimalathithan, K., Manoharan, J., Hirayama, S., Hayashi, S., and Combest, J., "Real world accident analysis of driver car-to-car intersection near-side impacts: focus on impact location, impact angle and lateral delta-V," *WCX World Congress Experience*, SAE Technical Paper, 2018.

16. Gabler, L.F., Crandall, J.R., and Panzer, M.B., "Development of a Second-Order System for Rapid Estimation of Maximum Brain Strain," *Ann. Biomed. Eng.* 47(9):1971–1981, 2019, doi:10.1007/s10439-018-02179-9.

17. Bandak, F., Eppinger, R., Haffner, M., Khaewpong, N., Kuppa, S., Maltese, M., Nguyen, T., Saul, R., Sun, E., Takhounts, E., and others, "Development of improved injury criteria for the assessment of advanced automotive restraint systems: II," United States. Department of Transportation. National Highway Traffic Safety Administration, 1999.

18. New Car Assessment Program, Federal Register Docket No. NHTSA-2015-0119, United States. Department of Transportation. National Highway Traffic Safety Administration: 78522–78591, 2015.

19. Petitjean, A., Trosseille, X., Petit, P., Irwin, A., Hassan, J., and Praxl, N., "Injury risk curves for the WorldSID 50th male dummy," SAE Technical Paper, 2009.

20. Kuppa, S., “Injury criteria for side impact dummies,” *Wash. DC Natl. Transp. Biomech. Res. Cent. Natl. Highw. Saftey Adm. US DOT* 67, 2004.

21. Rupp, J.D., Reed, M.P., Miller, C.S., Madura, N.H., Klinich, K.D., Kuppa, S.M., and Schneider, L.W., “Development of new criteria for assessing the risk of knee-thigh-hip injury in frontal impacts using Hybrid III femur force measurements,” *Proceedings of the 21st International Technical Conference on the Enhanced Safety of Vehicles (Paper 09-0306)*, 2009.

22. Kuppa, S., Wang, J., Haffner, M., and Eppinger, R., “Lower extremity injuries and associated injury criteria,” SAE Technical Paper, 2001.

23. Gehre, C. and Stahlschmidt, S., “Assessment of dummy models by using objective rating methods,” *22nd International Technical Conference on the Enhanced Safety of Vehicles (ESV) National Highway Traffic Safety Administration*, 2011.

24. International Organization for Standardization, “ISO/TS 18571:2024 Road vehicles—Objective rating metric for non-ambiguous signals,” ISO/TS 18571:2024, ISO, Geneva, Switzerland, 2024.

25. Thomas, P., Wozdin, E., Mackay, M., Cesari, D., Crandall, C., Gennarelli, T., Langwieder, K., Lovesund, P., Mclean, A.J., Mellander, H., Mohan, D., Ono, K., Otte, D., Walz, F., and Wismans, J., “Future research directions in injury biomechanics and passive safety research,” International Research Council on Biomechanics of Injury (IRCOBI), Madrid, Spain, 2006.

26. Paparrizos, J., Yang, F., and Li, H., “Bridging the gap: A decade review of time-series clustering methods,” *ArXiv Prepr. ArXiv241220582*, 2024.

27. Agnew, A.M., Sreedhar, A., Bolte IV, J.H., and Kang, Y.S., “Exploratory Comparison of Human Rib Structural Behavior in Two Dynamic Loading Scenarios,” *Conference proceedings International Research Council on the Biomechanics of Injury, IRCOBI*, 775–786, 2021.

28. Griffin, R., Huisingh, C., McGwin, G., and Reiff, D., “Association between side-impact airbag deployment and risk of injury,” *J. Trauma Acute Care Surg.* 73(4):914–918, 2012, doi:10.1097/TA.0b013e31825a7636.

29. Hallman, J.J., Yoganandan, N., and Pintar, F.A., “Door velocity and occupant distance affect lateral thoracic injury mitigation with side airbag,” *Accid. Anal. Prev.* 43(3):829–839, 2011, doi:10.1016/j.aap.2010.11.002.

30. Khouzam, R.N., Al-Mawed, S., Farah, V., and Mizeracki, A., “Next-Generation Airbags and the Possibility of Negative Outcomes Due to Thoracic Injury,” *Can. J. Cardiol.* 30(4):396–404, 2014, doi:10.1016/j.cjca.2014.01.002.

31. Kong, J.S., Lee, K.H., Kang, C.Y., Choi, D., and Kim, O.H., “Preventive Effectiveness of Thoracic Side Airbags in Side-Impact Crashes Based on Korea In-Depth Accident Study (KIDAS) Database,” *Int. J. Environ. Res. Public. Health* 19(23):15757, 2022, doi:10.3390/ijerph192315757.

32. Concepcion, J., Alfaro, S., Yeager, M., Newsome, K., Selvakumar, S., Andrade, R., Kornblith, L., Bilski, T., Ibrahim, J., and Elkbuli, A., “Analysis of biomechanics of motor vehicle collisions for passenger cars: implications for passenger vehicle safety and future car design innovations,” *J. Surg. Res.* 285:243–251, 2023.

33. Banglmaier, R.F., Rouhana, S.W., Beillas, P., and Yang, K.H., “Lower extremity injuries in lateral impact: a retrospective study.,” *Annu. Proc. Assoc. Adv. Automot. Med.* 47:425–44, 2003.

34. Morris, A., Welsh, R., Barnes, J., and Frampton, R., “The Nature, Type and Consequences of Lower Extremity Injuries in Front and Side Impacts in Pre- and Post-Regulatory Passenger Cars,” *2006 International IRCOBI Conference on the biomechanics of impact*, International Research Council on the Biomechanics of Impact (IRCOBI), 2006.

35. Arndt, N. and Grzebieta, R.H., “Lower extremity injuries in side-impact vehicle crashes,” *Int. J. Crashworthiness* 8(5):495–512, 2003, doi:10.1533/ijcr.2003.0255.

VIII. APPENDIX

Table A1

Distribution of occupants' height associated with L-type crashes

	Unweighted					Weighted				
Sex	Mean	S.D.	Q1	Q2	Q3	Mean	S.D.	Q1	Q2	Q3
Total	165	19.4	160	168	175	166	21.5	160	168	178
Male	172	21.9	170	178	183	173	21.7	173	178	183
Female	160	15.4	157	163	168	158	18.6	157	163	168

Table A2

Frequencies of regrouped vehicle types in L- and T-type crashes

	L-type crashes				T-type crashes			
Vehicle	Unweighted (n=376)		Weighted (n=223,340)		Unweighted (n=154)		Weighted (92,059)	
type	N	%	N	%	N	%	N	%
Sedan	228	60.7	129,253	57.9	110	71.4	68,198	74.1
SUV	96	25.5	75,011	33.6	32	20.8	13,714	14.9
LTV	52	13.8	19,076	8.5	12	7.8	10,147	11.0

Table A3

Comparison of MAIS2+ injury severity according to vehicle types in L-type crashes

	Unweighted (n=376)				Weighted (n=223,340)			
Vehicle	MAIS<2 (n=332)		MAIS2+ (n=44)		MAIS<2 (n=204,808)		MAIS2+ (n=18,532)	
type	N	%	N	%	N	%	N	%
Sedan	197	86.4	31	13.6	113,223	87.6	16,030	12.4
SUV	89	92.7	7	7.3	73,474	98.0	1,537	2.0
LTV	46	88.5	6	11.5	18,111	94.9	965	5.1

Table A4

Comparison of MAIS3+ injury severity according to vehicle types in L-type crashes

	Unweighted (n=376)				Weighted (n=223,340)			
Vehicle	MAIS<3 (n=362)		MAIS3+ (n=14)		MAIS<3 (n=210,684)		MAIS3+ (n=12,657)	
type	N	%	N	%	N	%	N	%
Sedan	220	96.5	8	3.5	117,224	90.7	12,030	9.3
SUV	92	95.8	4	4.2	74,564	99.4	447	0.6
LTV	50	96.2	2	3.8	18,896	99.1	180	0.9

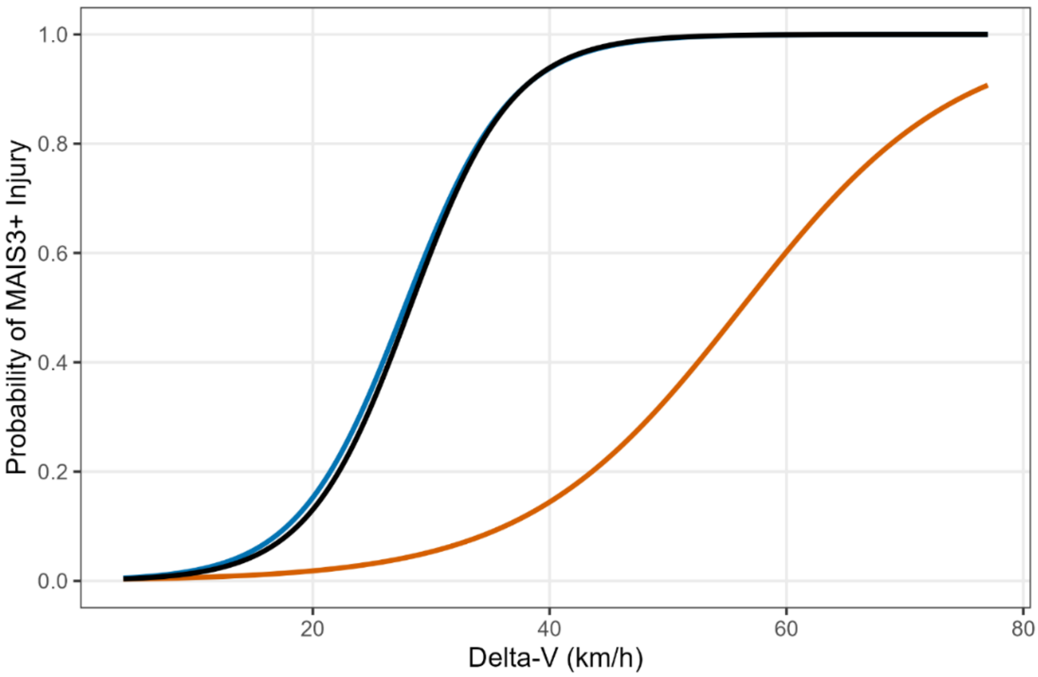

Fig. A1. Injury risk in MAIS3+ severity according to vehicle type in L-type crashes
Sedans (Blue), SUVs (Orange), All vehicle types (Black)

Table A5
Delta-V at 50% predicted probability of MAIS3+ injury risk by vehicle type

Vehicle type	Target probability	Delta V at target probability
Sedan	0.5	27.7
SUV	0.5	56.2
All vehicle types	0.5	28.2

Table A6

Time History Evaluation of Physical Test Against Simulation Hybrid III 50th Male ATD Signals

		CORA [23]				ISO/TS 18571:2024 [24]			
	Signal	Progression	Phase	Size	**Total**	Slope	Phase	Magnitude	**Total**
Driver	Head Ax [g]	0.700	0.856	0.753	**0.752**	0.871	0.791	0.449	**0.720**
	Head Ay [g]	0.670	0.863	0.412	**0.654**	0.875	0.410	0.424	**0.602**
	Head Az [g]	0.008	0.129	0.434	**0.145**	0.472	0.197	0.123	**0.324**
	Head Ares [g]	0.736	0.937	0.865	**0.818**	0.964	0.823	0.440	**0.776**
	Average	0.529	0.696	0.616	0.592	0.796	0.555	0.359	0.606
Passenger	Head Ax [g]	0.937	0.474	0.951	**0.825**	0.665	0.913	0.468	**0.699**
	Head Ay [g]	0.967	0.577	0.698	**0.802**	0.718	0.871	0.504	**0.701**
	Head Az [g]	0.813	0.790	0.478	**0.723**	0.831	0.759	0.279	**0.577**
	Head Ares [g]	0.942	0.907	0.717	**0.877**	0.899	0.900	0.319	**0.717**
	Neck Fx [N]	0.946	0.401	0.996	**0.822**	0.621	0.936	0.471	**0.680**
	Neck Fy [N]	0.979	0.511	0.618	**0.772**	0.673	0.809	0.553	**0.656**
	Neck Fz [N]	0.833	0.775	0.533	**0.743**	0.823	0.775	0.235	**0.577**
	Neck My [Nm]	0.526	0.000	0.490	**0.385**	0.335	0.556	0.344	**0.388**
	Chest Ax [g]	0.683	0.834	0.889	**0.772**	0.863	0.688	0.443	**0.690**
	Chest Ay [g]	0.871	1.000	0.983	**0.931**	0.968	0.874	0.444	**0.785**
	Chest Az [g]	0.056	0.000	0.242	**0.088**	0.000	0.258	0.327	**0.313**
	Chest Ares [g]	0.905	0.937	0.903	**0.912**	0.915	0.887	0.486	**0.809**
	PV Ax [g]	0.780	0.665	0.855	**0.770**	0.766	0.795	0.182	**0.605**
	PV Ay [g]	0.879	0.944	0.976	**0.919**	0.919	0.917	0.334	**0.763**
	PV Az [g]	0.533	0.210	0.281	**0.389**	0.516	0.358	0.277	**0.453**
	PV Ares [g]	0.935	0.746	0.908	**0.881**	0.823	0.929	0.316	**0.754**
	L. Fem. Fz [N]	0.543	0.000	0.094	**0.295**	0.722	0.000	0.055	**0.199**
	R. Fem. Fz [N]	0.866	0.525	0.302	**0.640**	0.685	0.448	0.027	**0.412**
	Lap Belt F [N]	0.921	0.900	0.614	**0.839**	0.891	0.789	0.245	**0.645**
	Sho. Belt F [N]	0.845	0.878	0.643	**0.803**	0.883	0.732	0.152	**0.605**
	Average	0.795	0.598	0.672	0.715	0.723	0.719	0.330	0.606

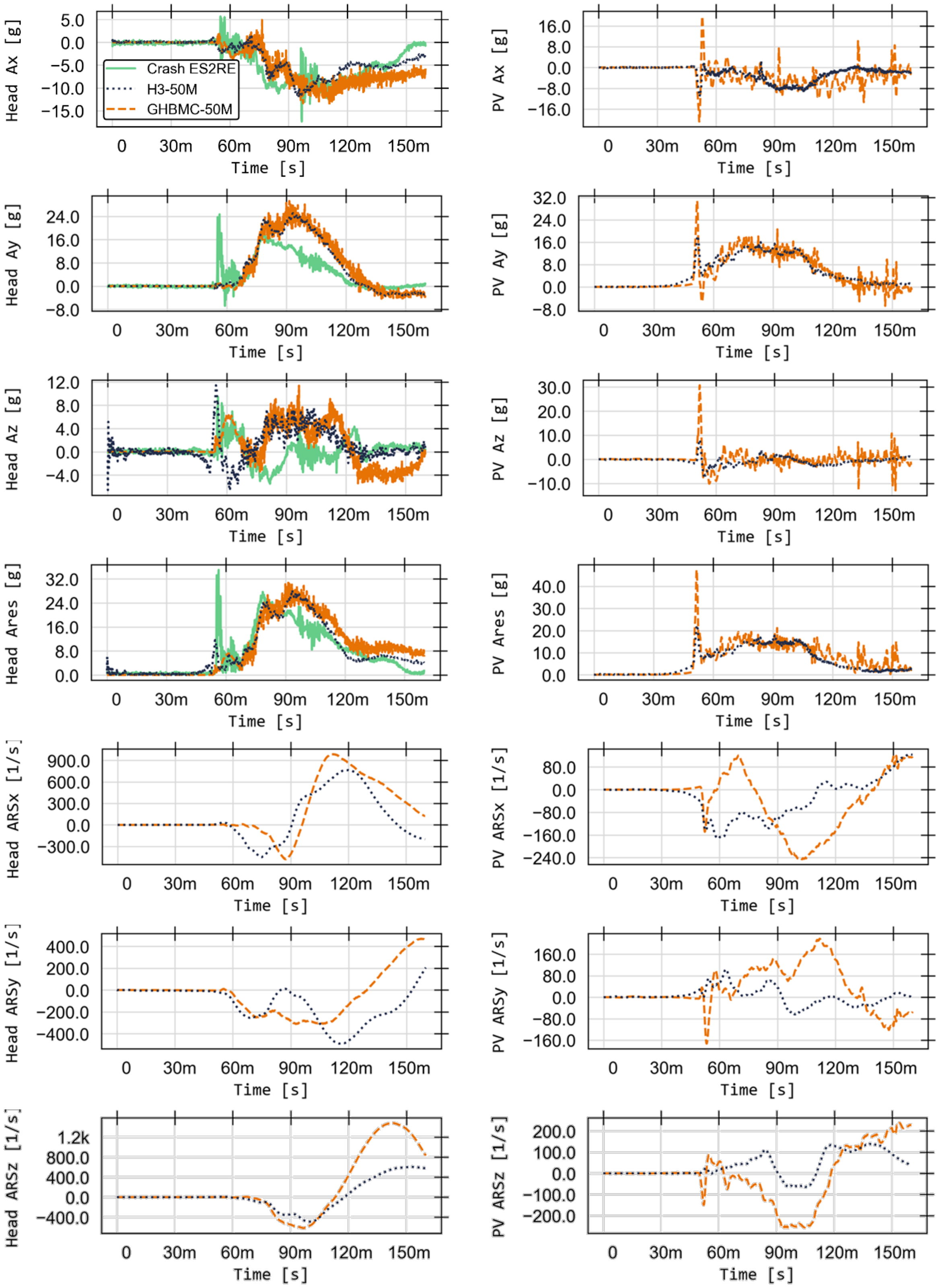

Fig. A2. Driver Occupant Model Time History Signals of Kinematic and Loading Instrumentation for Baseline Pulse (Part I): Crash ES2RE ATD (Green Solid), H3-50M Model (Blue Dotted), GHBMC-50M (Orange Dashed)

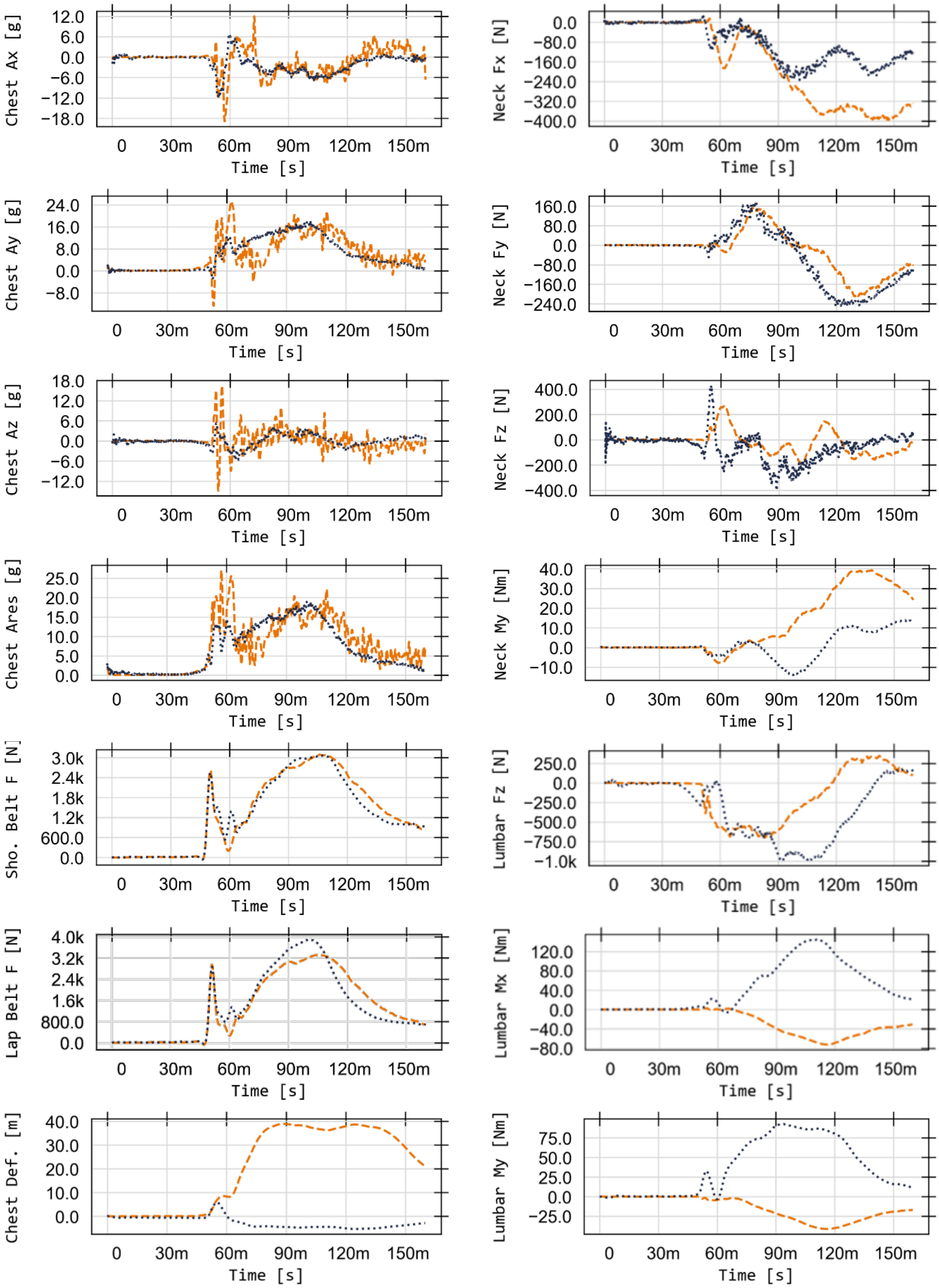

Fig. A3. Driver Occupant Model Time History Signals of Kinematic and Loading Instrumentation for Baseline Pulse (Part II): Crash ES2RE ATD (Green Solid), H3-50M Model (Blue Dotted), GHBMC-50M (Orange Dashed)

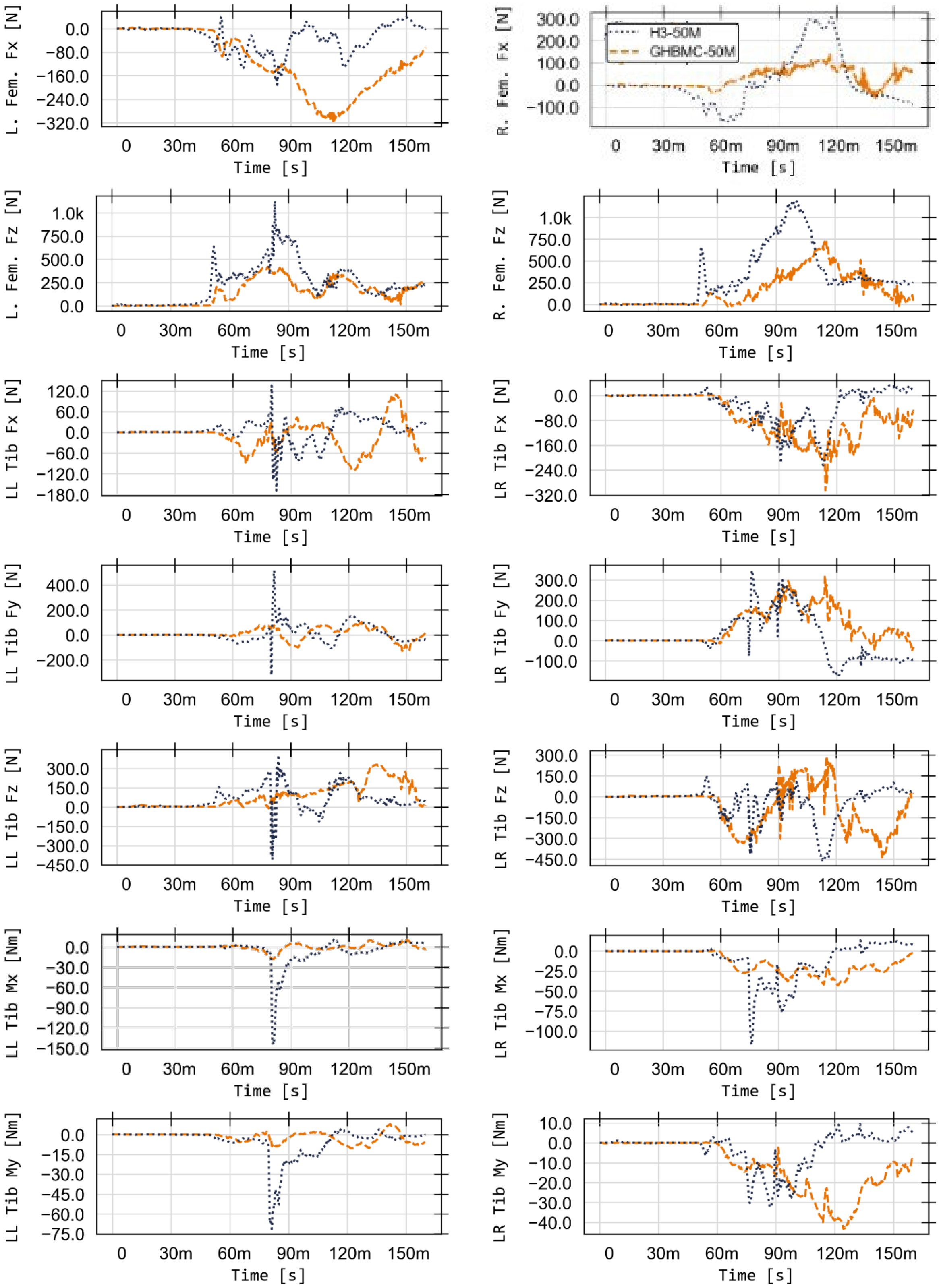

Fig. A4. Driver Occupant Model Time History Signals of Kinematic and Loading Instrumentation for Baseline Pulse (Part III): Crash ES2RE ATD (Green Solid), H3-50M Model (Blue Dotted), GHBMC-50M (Orange Dashed)

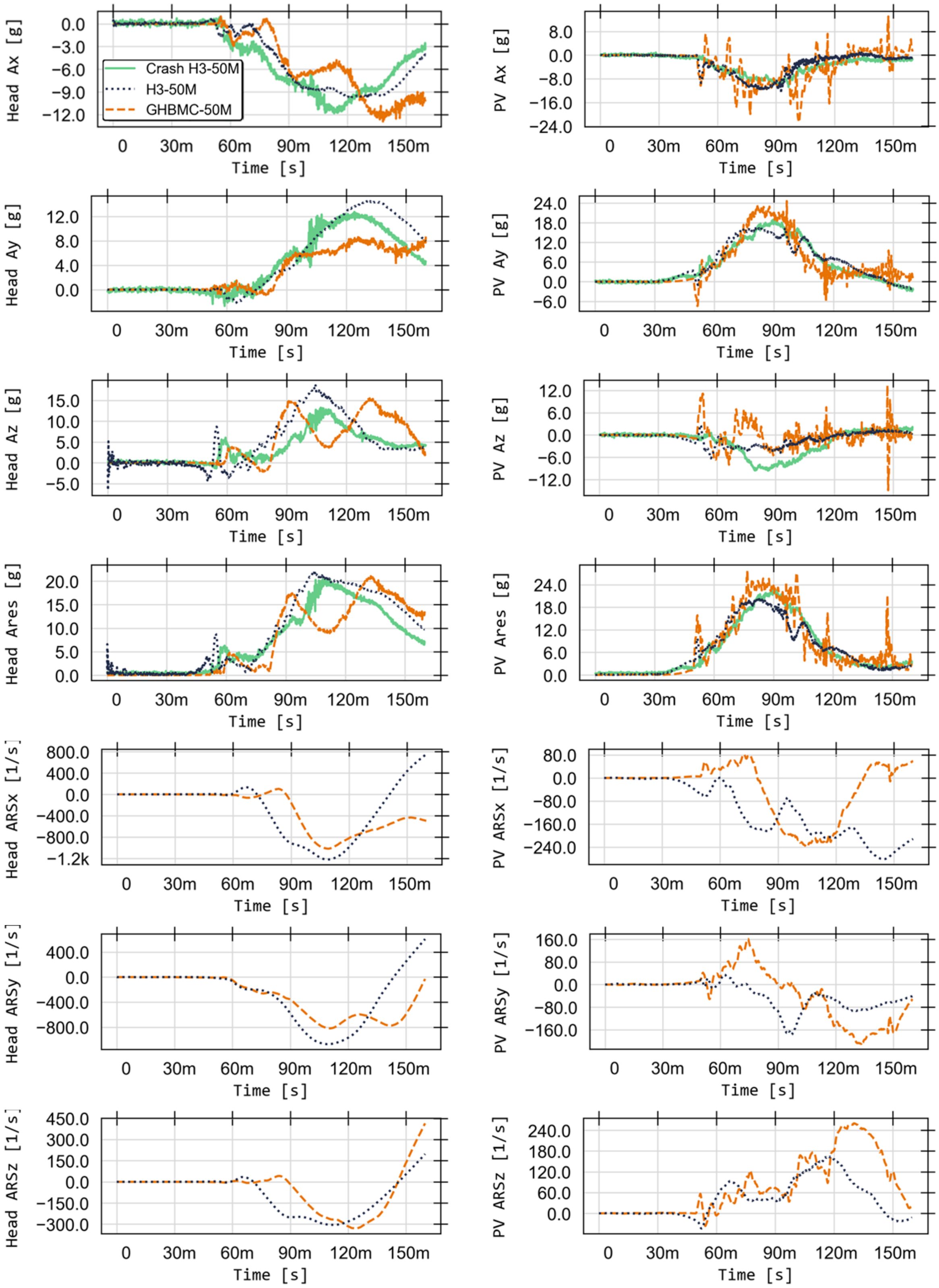

Fig. A5. Passenger Occupant Model Time History Signals of Kinematic and Loading Instrumentation for Baseline Pulse (Part I): Crash H3-50M ATD (Green Solid), H3-50M Model (Blue Dotted), GHBMC-50M (Orange Dashed)

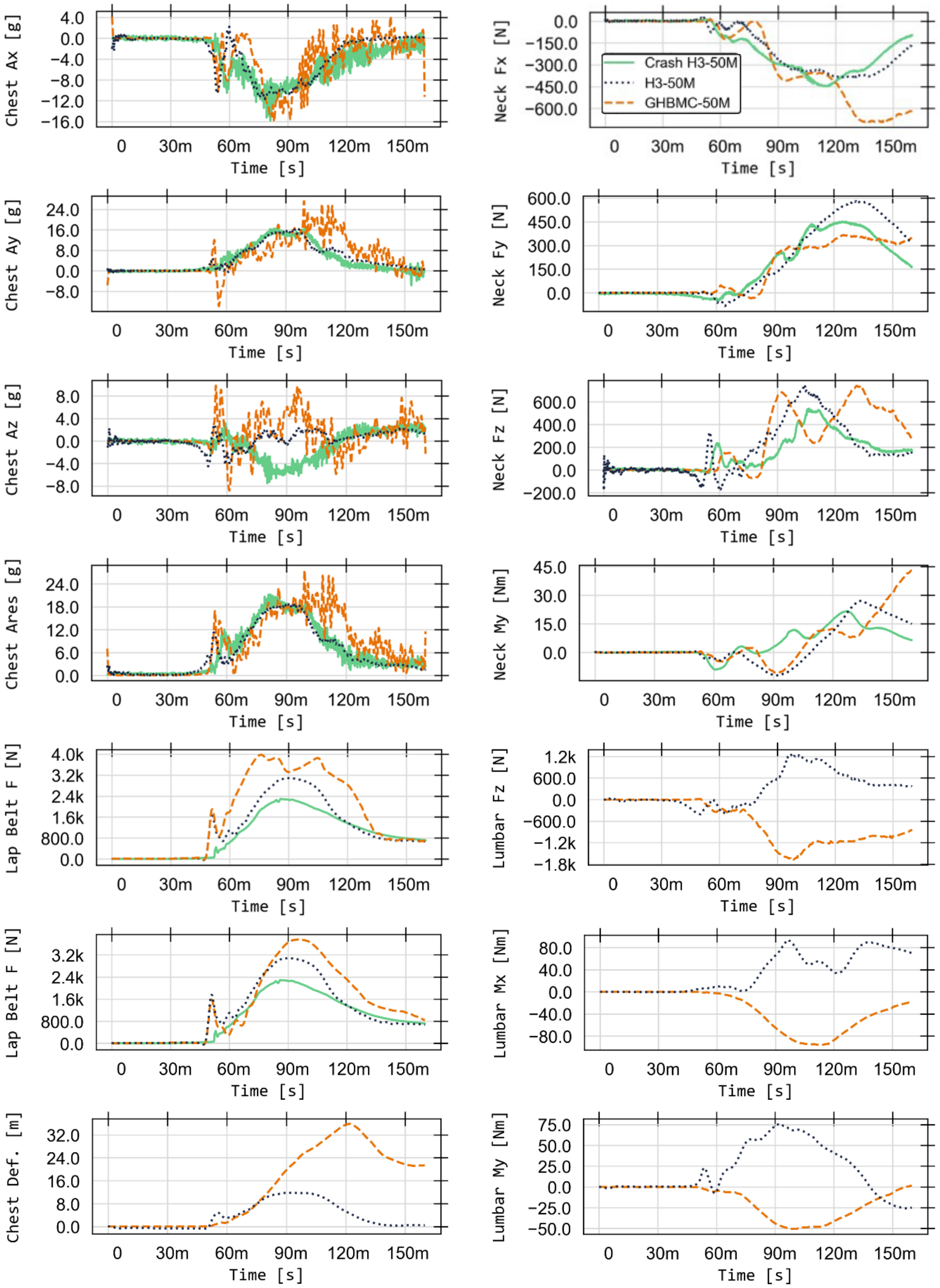

Fig. A6. Passenger Occupant Model Time History Signals of Kinematic and Loading Instrumentation for Baseline Pulse (Part II): Crash H3-50M (Green Solid), H3-50M Model (Blue Dotted), GHBMC-50M (Orange Dashed)

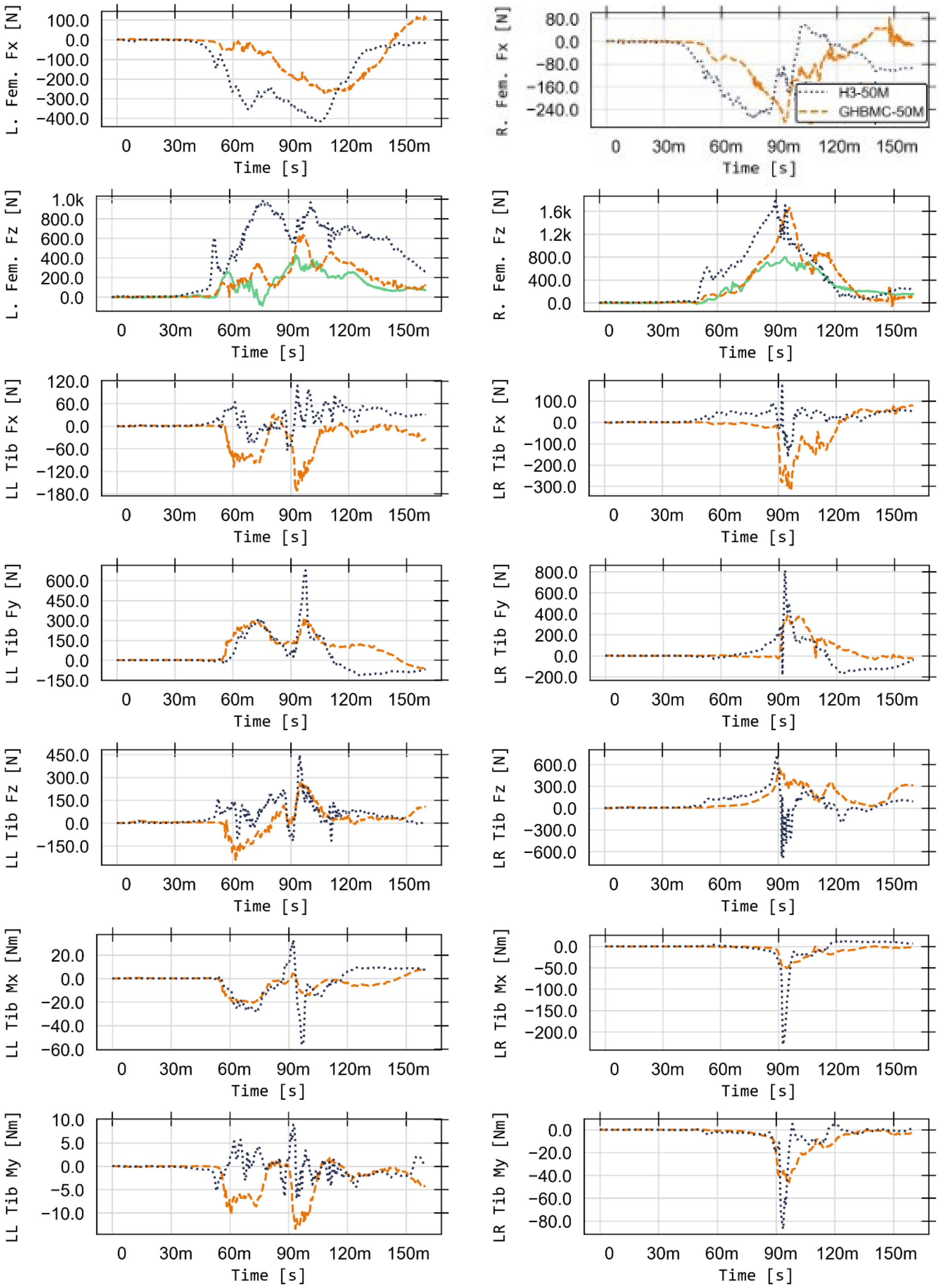

Fig. A7. Passenger Occupant Model Time History Signals of Kinematic and Loading Instrumentation for Baseline Pulse (Part III): Crash H3-50M (Green Solid), H3-50M Model (Blue Dotted), GHBMC-50M (Orange Dashed)

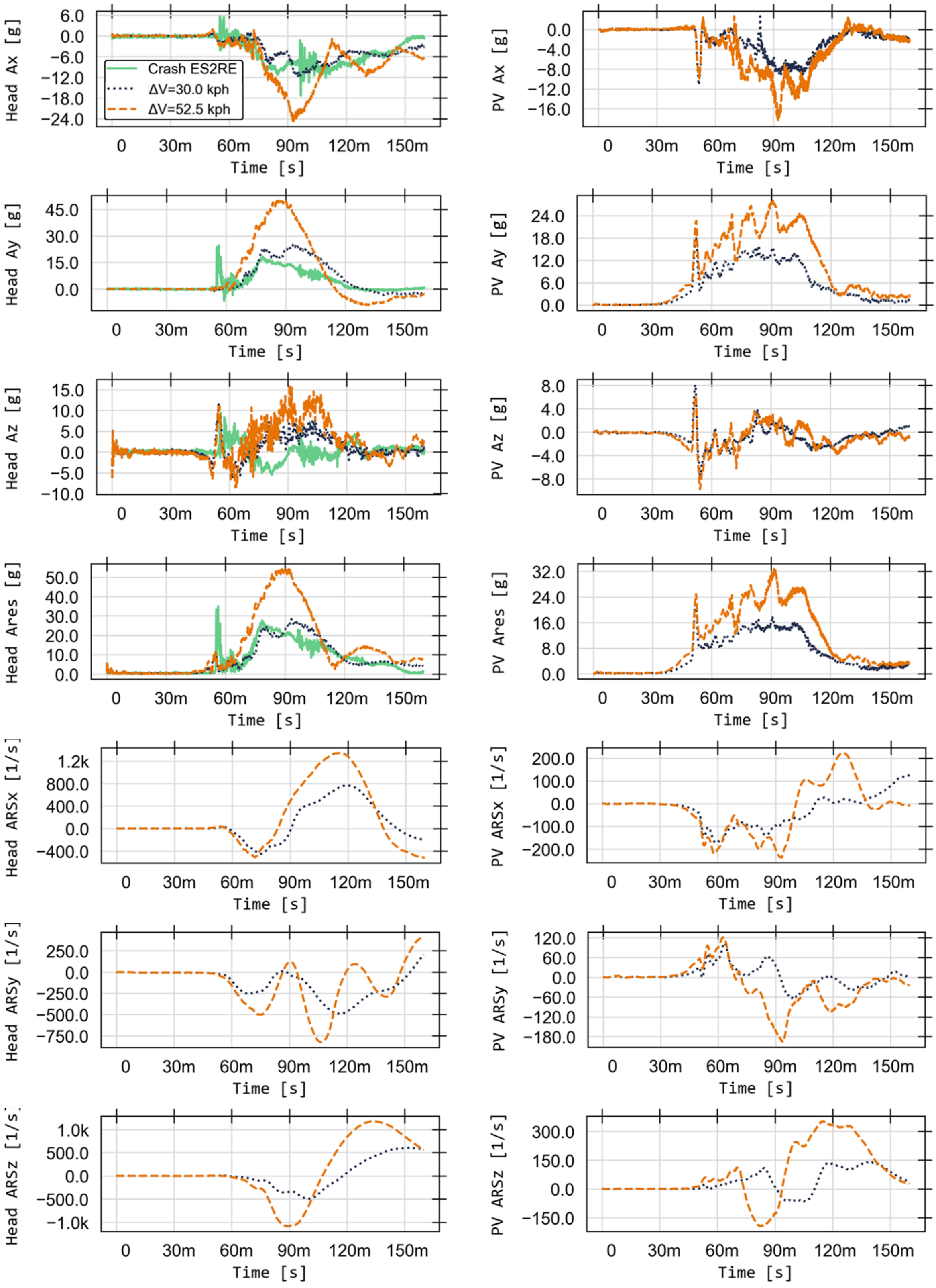

Fig. A8. H3-50M ATD Driver Occupant Model Time History Signals of Kinematic and Loading Instrumentation Pulse Severity Variation (Part I): Crash ES2RE ATD (Green Solid), ΔV=30.0 km/h (Blue Dotted), ΔV=52.5 km/h (Orange Dashed)

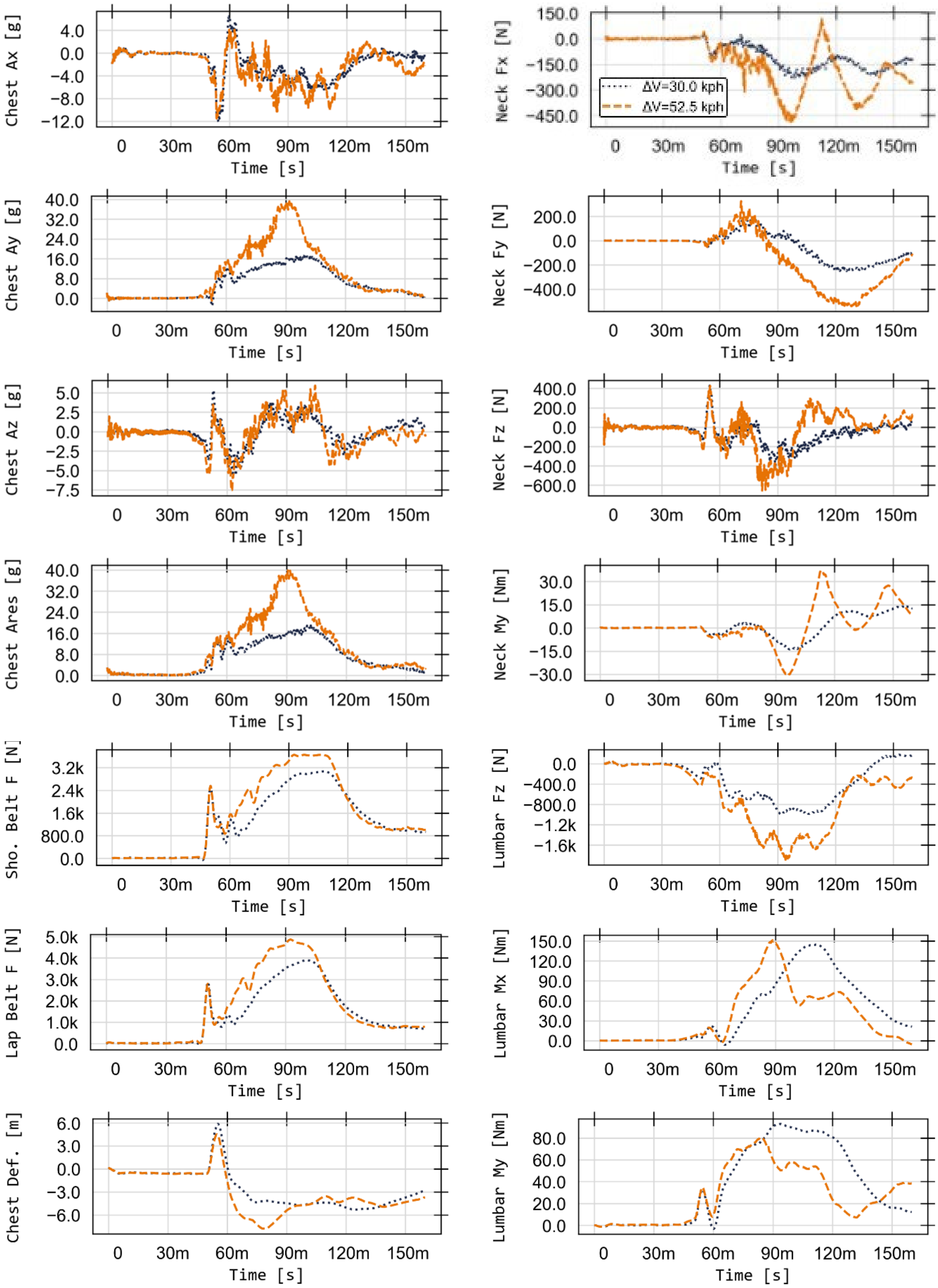

Fig. A9. H3-50M ATD Driver Occupant Model Time History Signals of Kinematic and Loading Instrumentation Pulse Severity Variation (Part II): Crash ES2RE ATD (Green Solid), ΔV=30.0 km/h (Blue Dotted), ΔV=52.5 km/h (Orange Dashed)

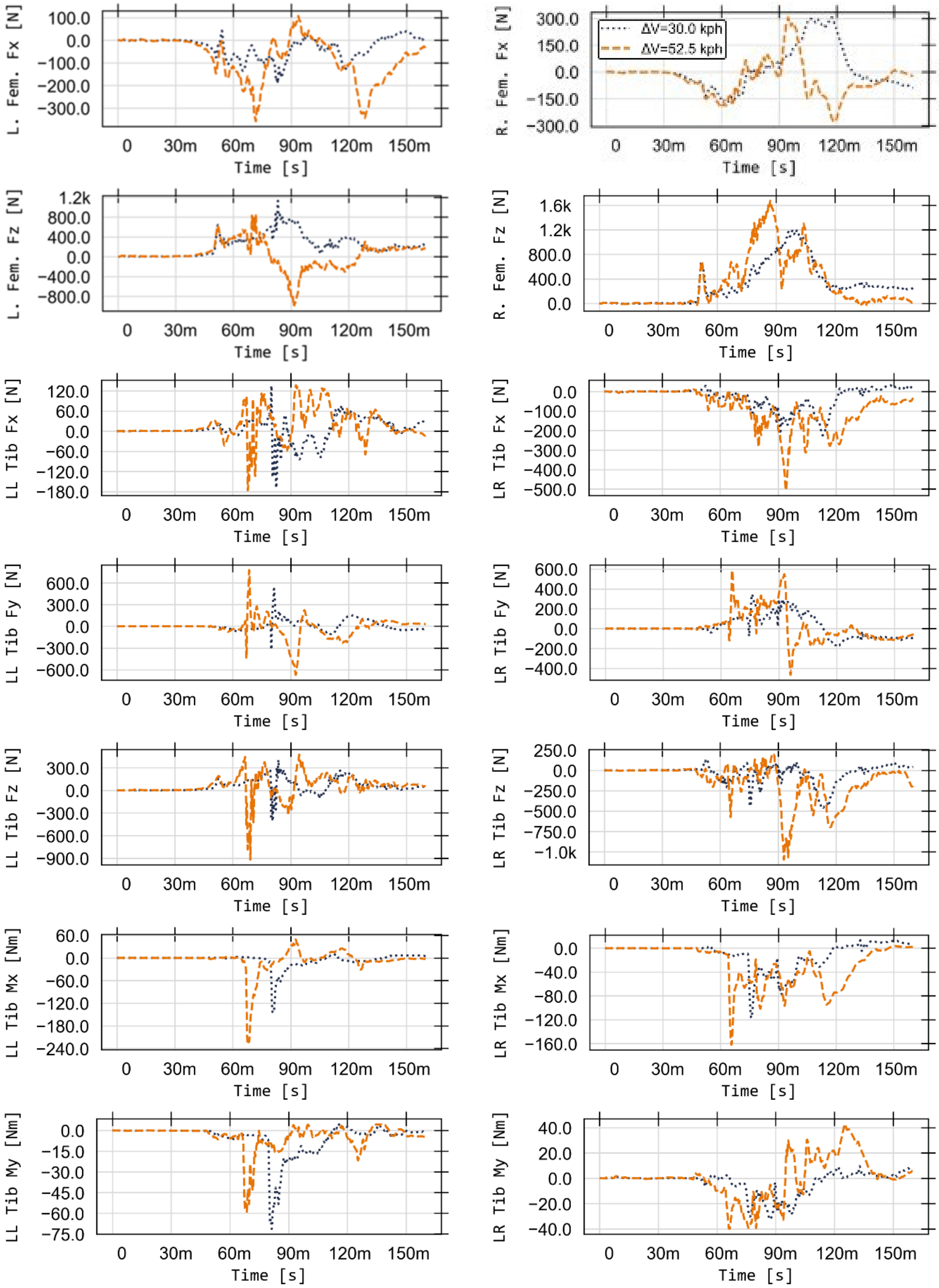

Fig. A10. H3-50M ATD Driver Occupant Model Time History Signals of Kinematic and Loading Instrumentation Pulse Severity Variation (Part III): Crash ES2RE ATD (Green Solid), ΔV=30.0 km/h (Blue Dotted), ΔV=52.5 km/h (Orange Dashed)

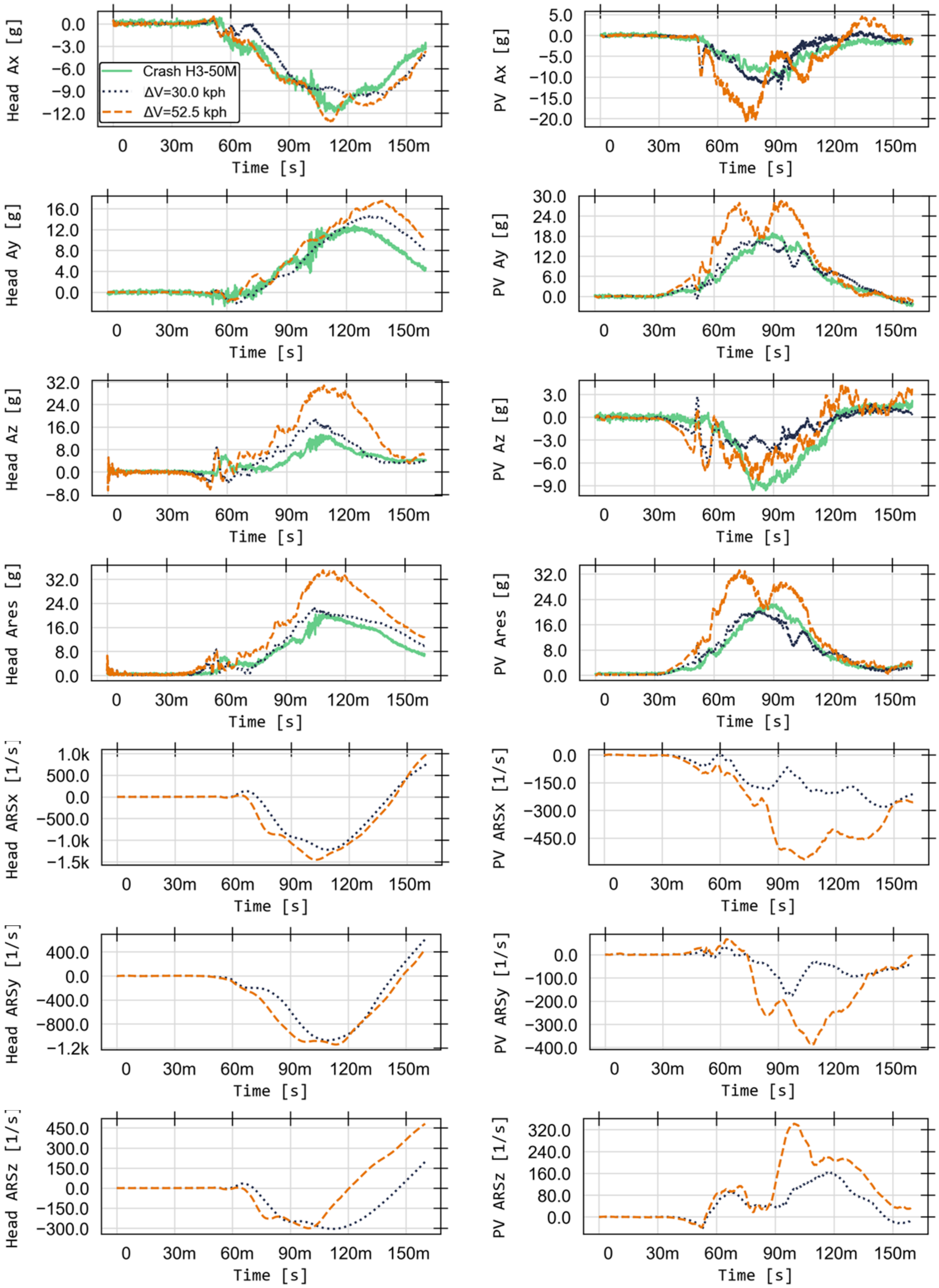

Fig. A11. H3-50M ATD Passenger Occupant Model Time History Signals of Kinematic and Loading Instrumentation Pulse Severity Variation (Part I): Crash ES2RE ATD (Green Solid), ΔV=30.0 km/h (Blue Dotted), ΔV=52.5 km/h (Orange Dashed)

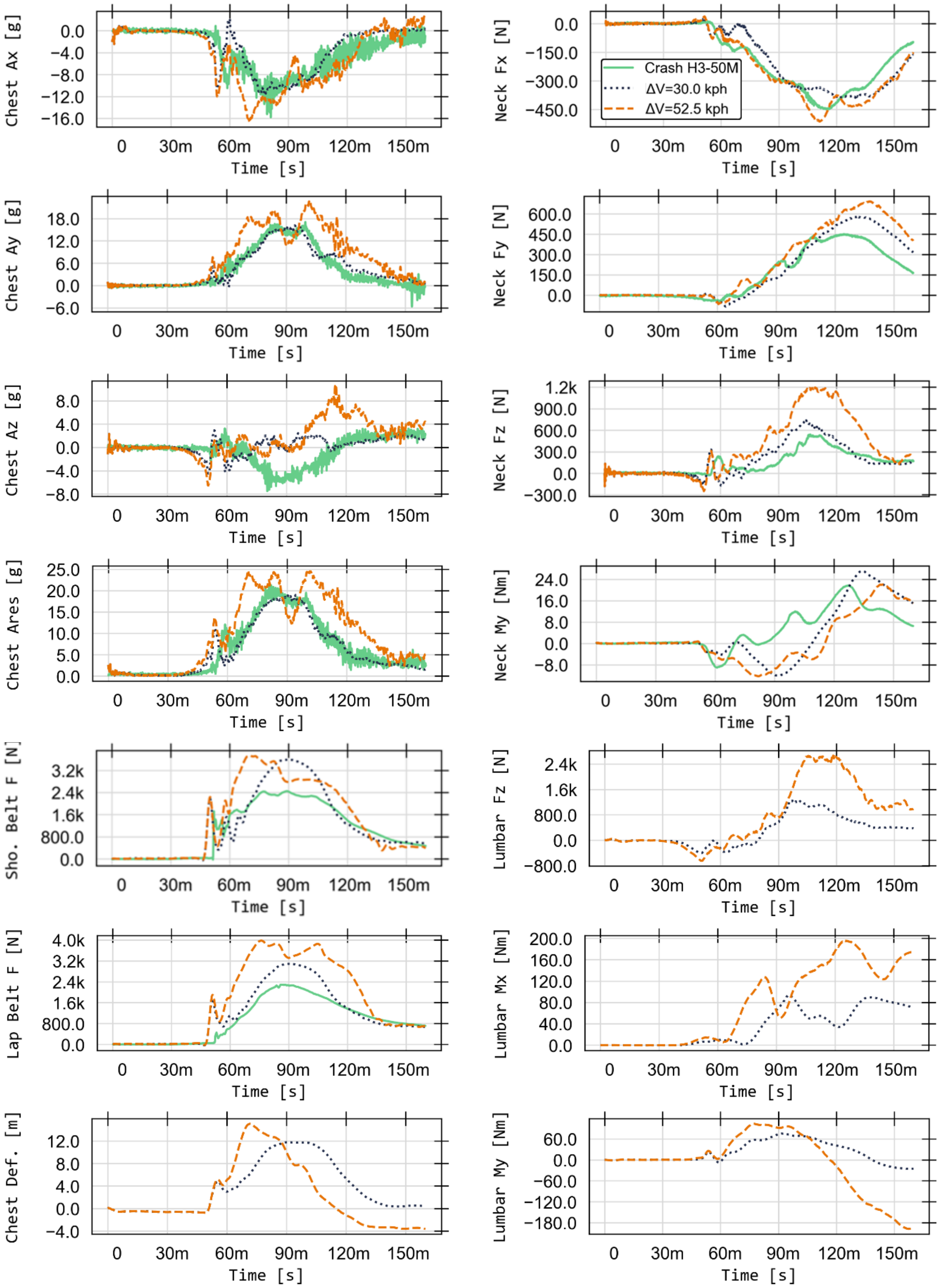

Fig. A12. H3-50M ATD Passenger Occupant Model Time History Signals of Kinematic and Loading Instrumentation Pulse Severity Variation (Part II): Crash ES2RE ATD (Green Solid), ΔV=30.0 km/h (Blue Dotted), ΔV=52.5 km/h (Orange Dashed)

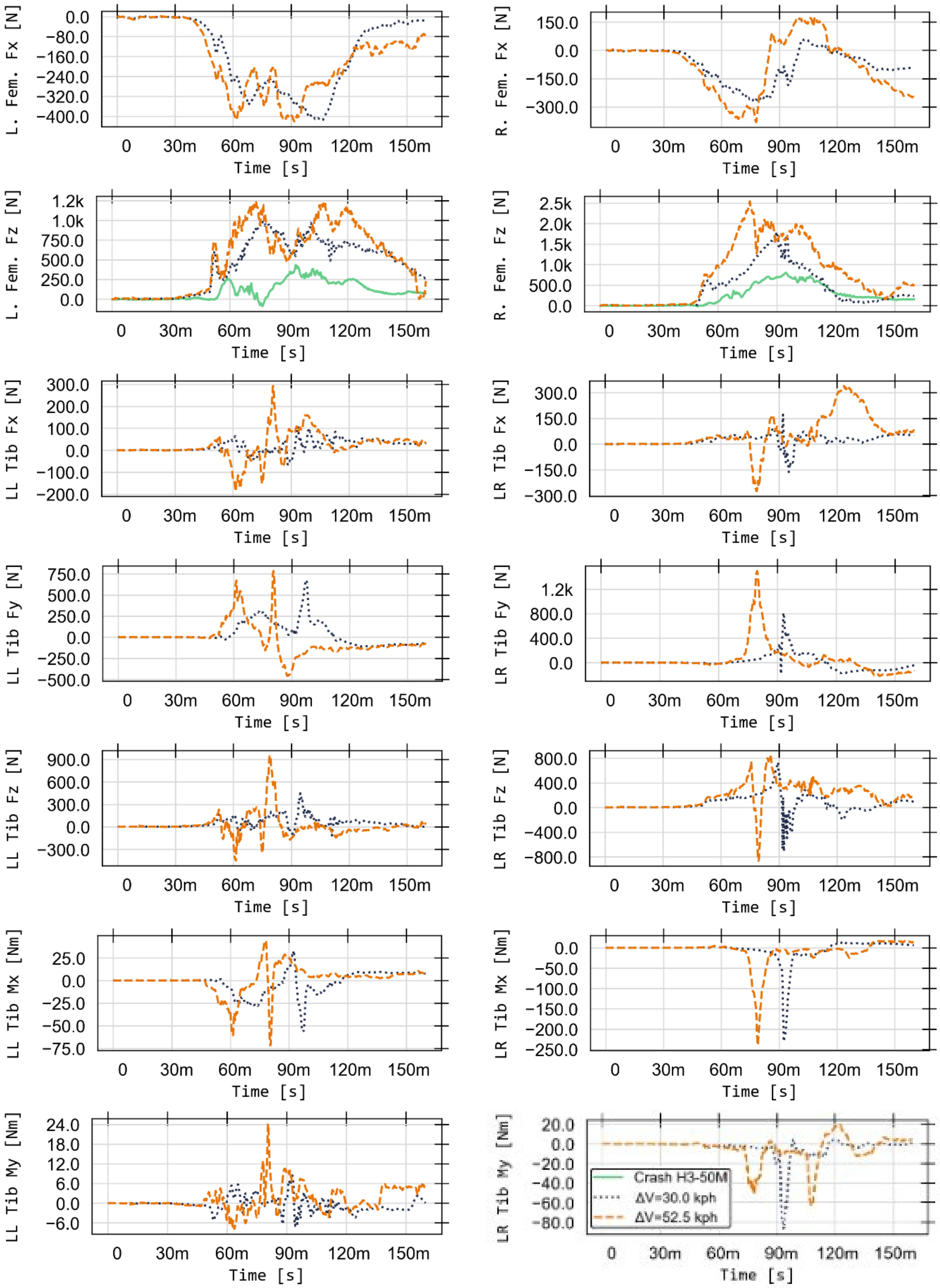

Fig. A13. H3-50M ATD Passenger Occupant Model Time History Signals of Kinematic and Loading Instrumentation Pulse Severity Variation (Part III): Crash ES2RE ATD (Green Solid), ΔV=30.0 km/h (Blue Dotted), ΔV=52.5 km/h (Orange Dashed)

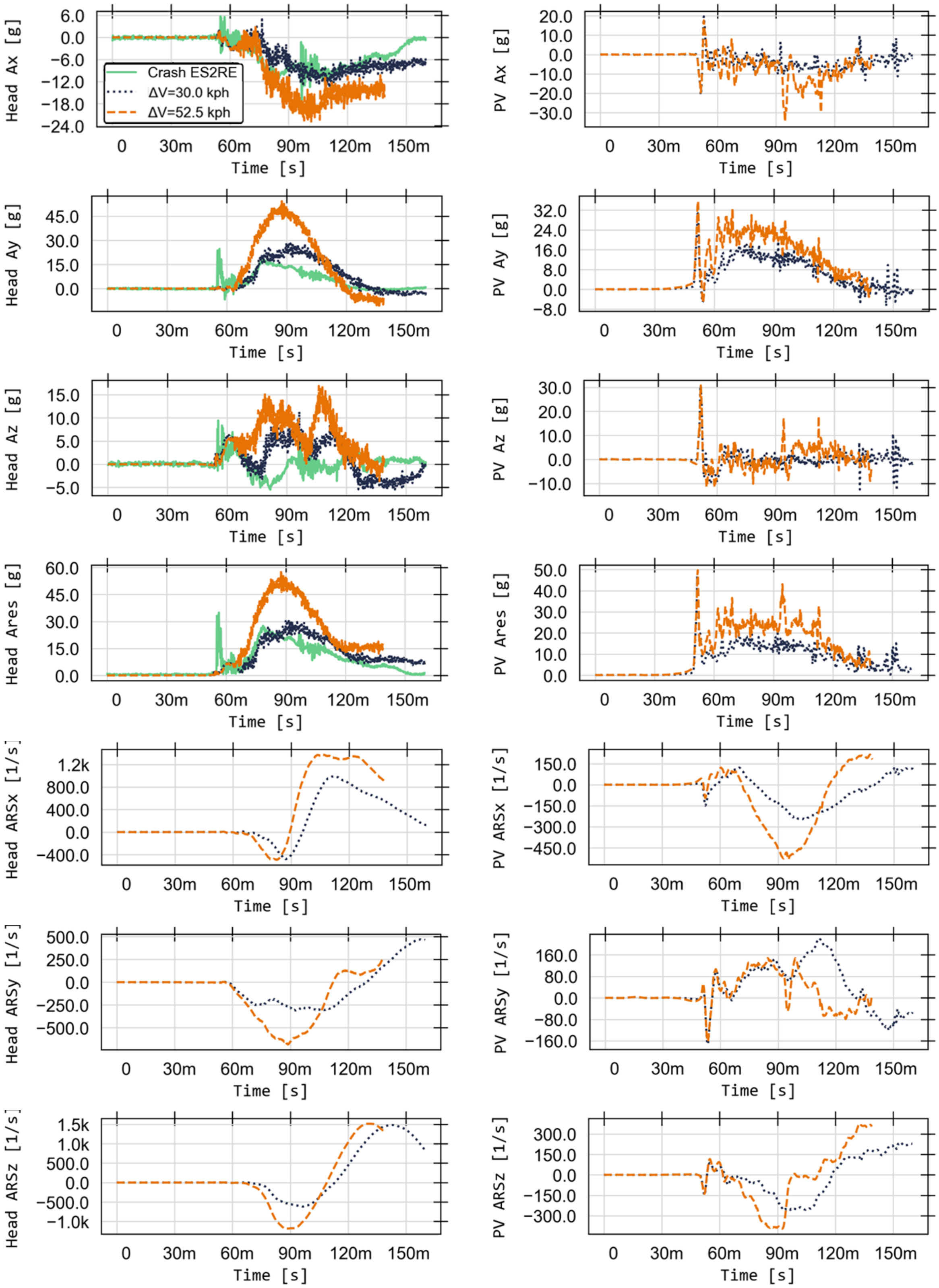

Fig. A14. GHBMC-50M HBM Driver Occupant Model Time History Signals of Kinematic and Loading Instrumentation Pulse Severity Variation (Part I): Crash ES2RE ATD (Green Solid), ΔV=30.0 km/h (Blue Dotted), ΔV=52.5 km/h (Orange Dashed)

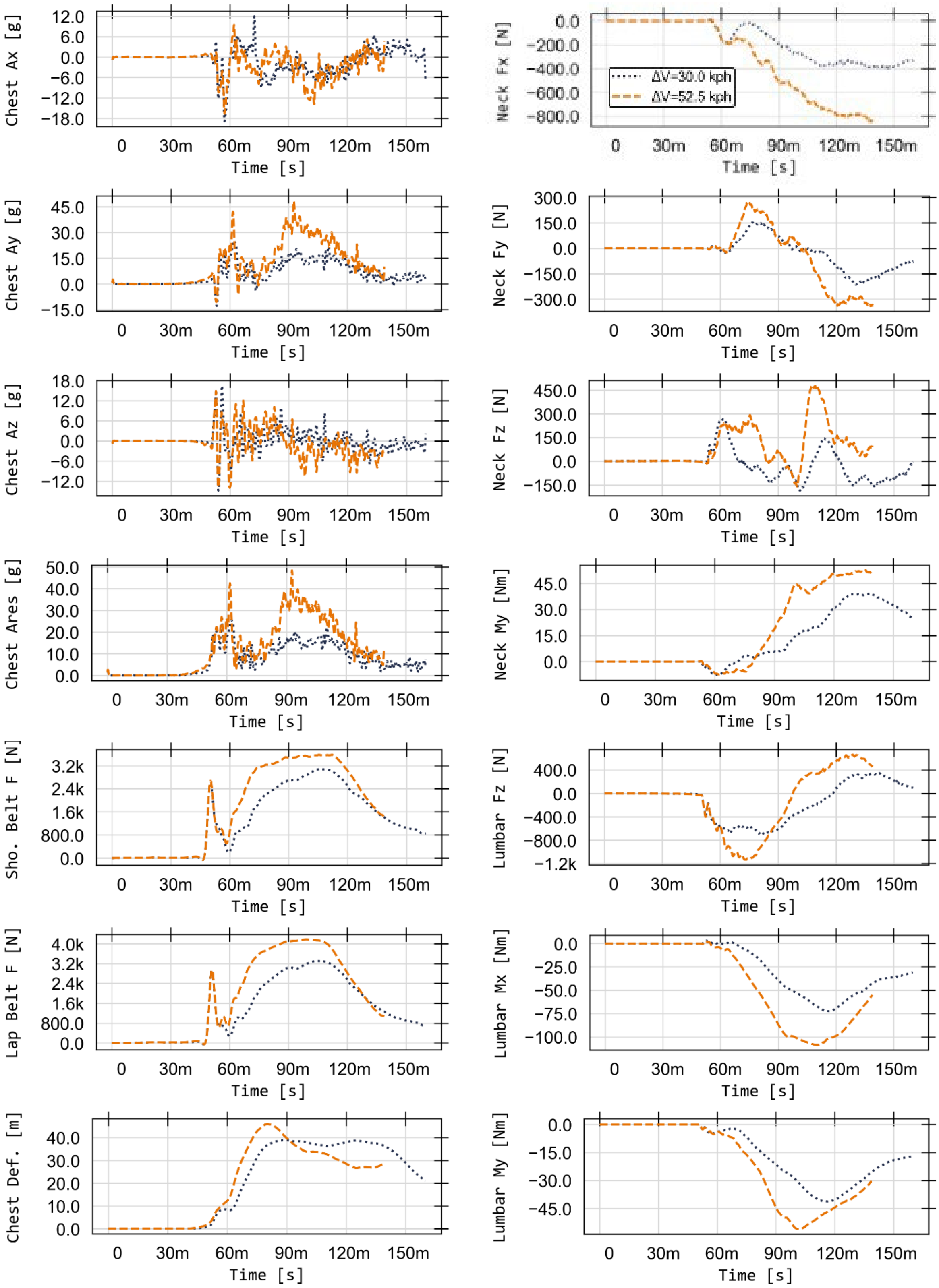

Fig. A15. GHBMC-50M HBM Driver Occupant Model Time History Signals of Kinematic and Loading Instrumentation Pulse Severity Variation (Part II): Crash ES2RE ATD (Green Solid), ΔV=30.0 km/h (Blue Dotted), ΔV=52.5 km/h (Orange Dashed)

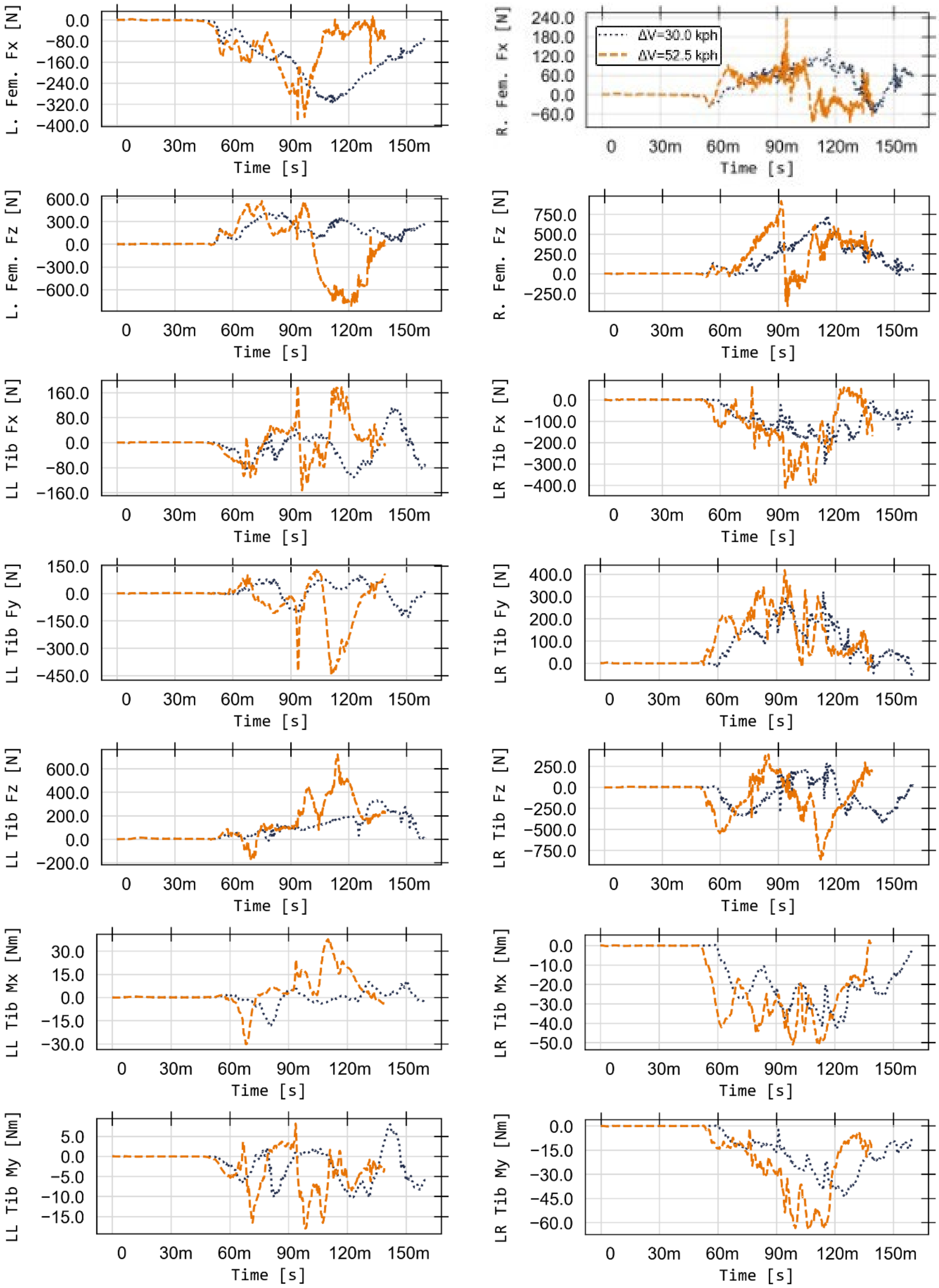

Fig. A16. GHBMC-50M HBM Driver Occupant Model Time History Signals of Kinematic and Loading Instrumentation Pulse Severity Variation (Part III): Crash ES2RE ATD (Green Solid), ΔV=30.0 km/h (Blue Dotted), ΔV=52.5 km/h (Orange Dashed)

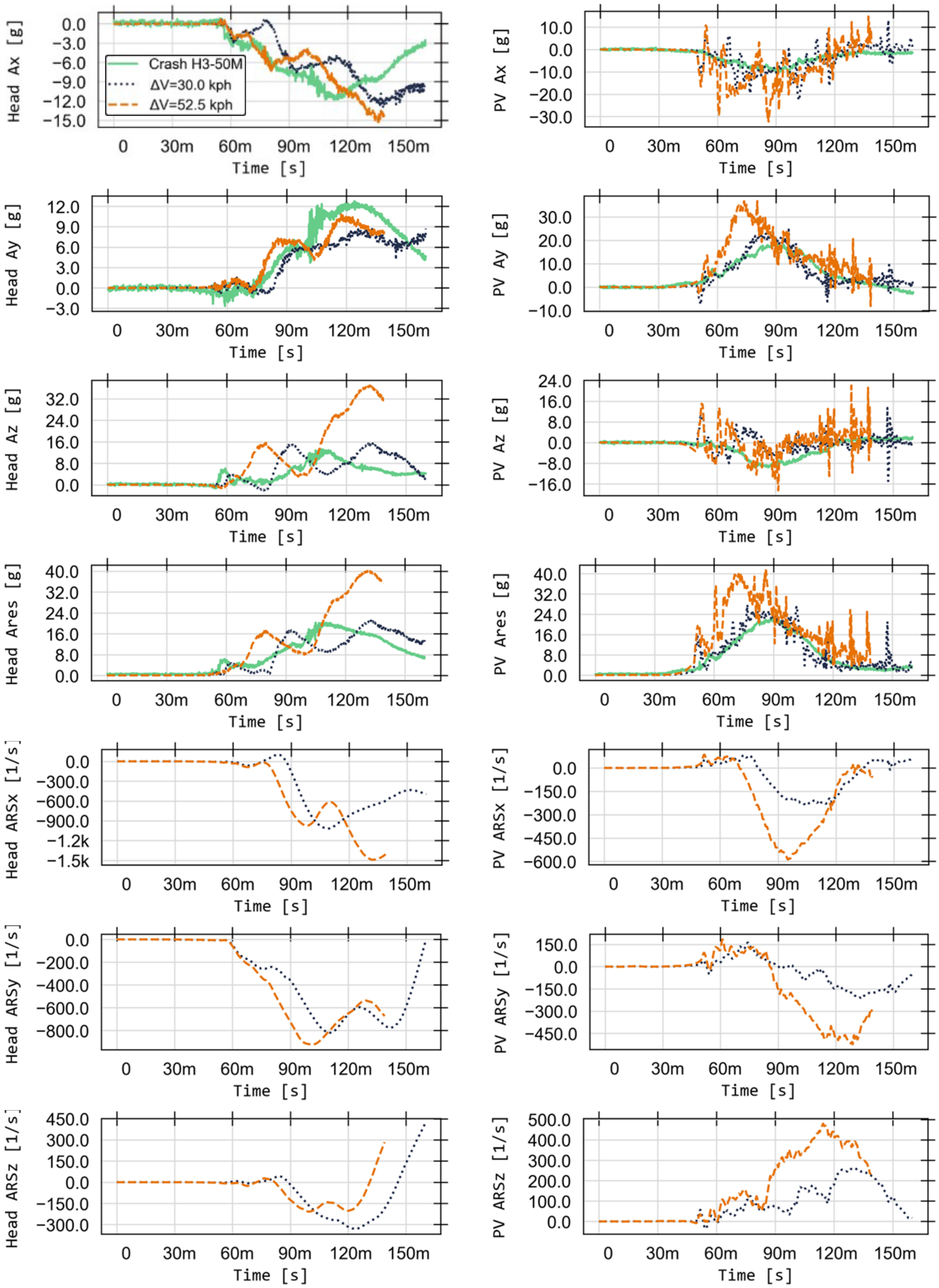

Fig. A17. GHBMC-50M HBM Passenger Occupant Model Time History Signals of Kinematic and Loading Instrumentation Pulse Severity Variation (Part I): Crash ES2RE ATD (Green Solid), ΔV=30.0 km/h (Blue Dotted), ΔV=52.5 km/h (Orange Dashed)

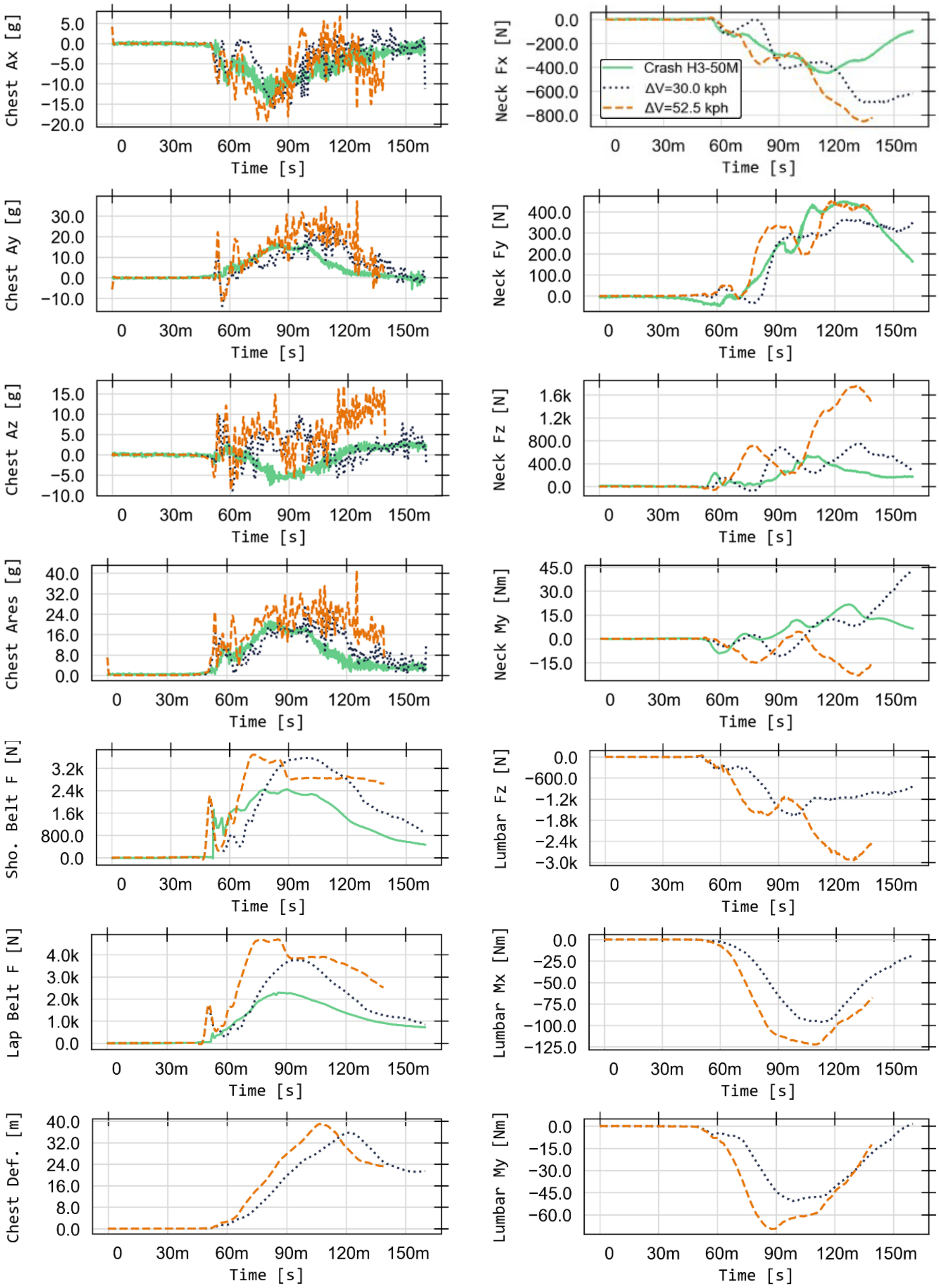

Fig. A18. GHBMC-50M HBM Passenger Occupant Model Time History Signals of Kinematic and Loading Instrumentation Pulse Severity Variation (Part II): Crash ES2RE ATD (Green Solid), ΔV=30.0 km/h (Blue Dotted), ΔV=52.5 km/h (Orange Dashed)

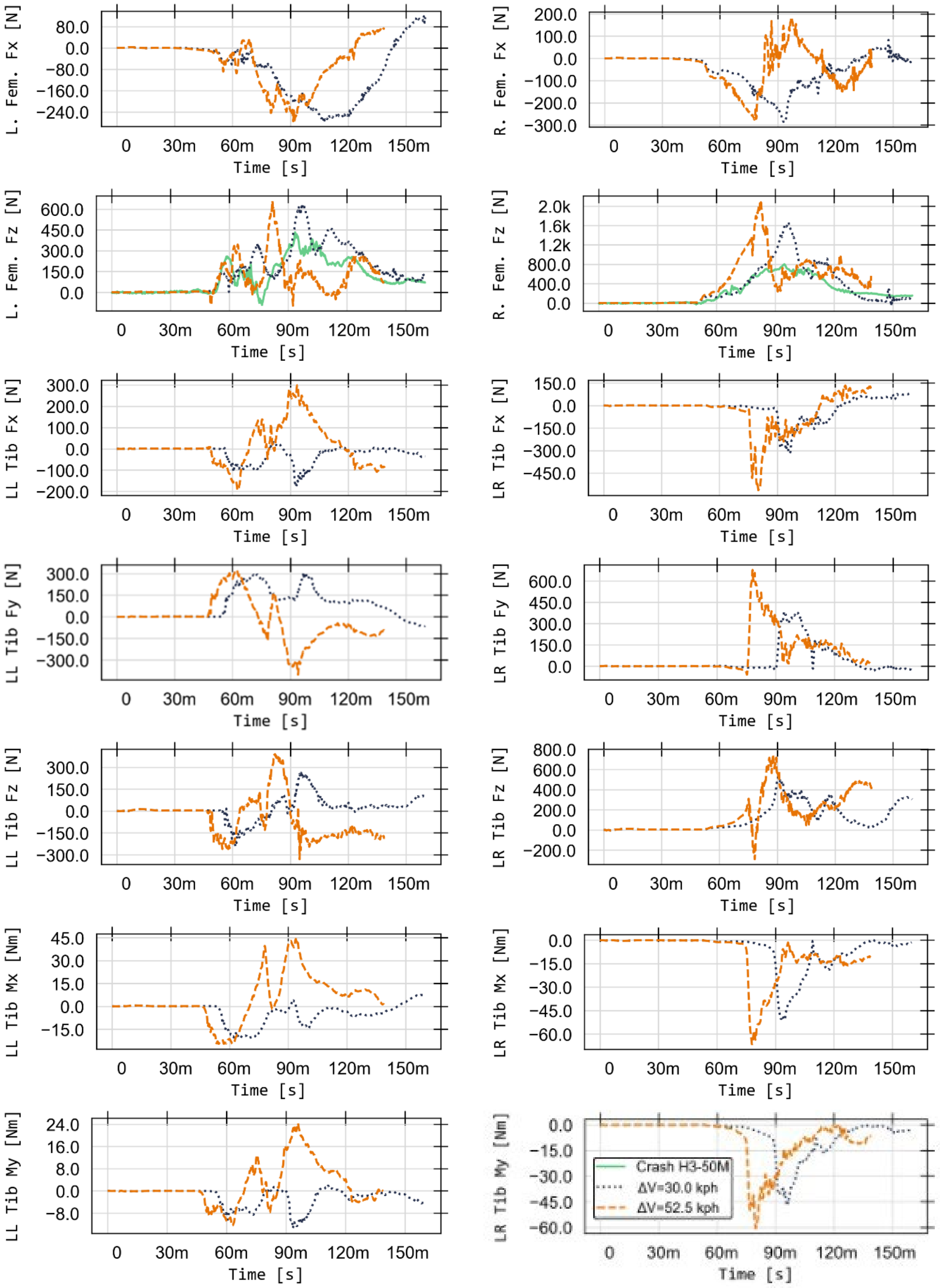

Fig. A19. GHBMC-50M HBM Passenger Occupant Model Time History Signals of Kinematic and Loading Instrumentation Pulse Severity Variation (Part III): Crash ES2RE ATD (Green Solid), ΔV=30.0 km/h (Blue Dotted), ΔV=52.5 km/h (Orange Dashed)